Mineralium Deposita (2023) 58:263–286
https://doi.org/10.1007/s00126-022-01120-4

ARTICLE

Bi/Te control on gold mineralizing processes in the North China Craton: Insights from the Wulong gold deposit

Haoxuan Feng[1,2,3] · Ping Shen[1,2,3] · Rixiang Zhu[4,3] · Andrew G. Tomkins[5] · Joël Brugger[5] · Ge Ma[1] · Changhao Li[1,3] · Yang Wu[1,2,3]

Received: 3 January 2021 / Accepted: 27 April 2022 / Published online: 2 June 2022

Abstract

The Wulong gold deposit (> 80 t Au) is located at the northeastern margin of the North China Craton (NCC). Gold in the most economically important quartz veins (Stages 2 and 3) is associated with a varied assemblage of Bi and Te minerals. Stage 2 is characterized by, in a temporal order, native gold-native bismuth-maldonite-hedleyite, bismuthinite-Bi-sulfotellurides, electrum-hessite-Bi-Pb-Ag sulfosalts, Bi-Pb sulfosalts, and Bi-Pb-sulfotellurides. All of these minerals except maldonite, electrum, hessite, and Bi-sulfosalts are present in Stage 3 veins, which also contain jonassonite and unnamed minerals with stoichiometry of Bi_8Te_3 and Bi_5Te_3. These complex Bi mineral assemblages resulted from changes in Pb, Ag, Te and Bi concentrations in reduced hydrothermal fluids both locally and temporally, from Stage 2 to 3. Texturally, approximately 85% of the gold grains are associated with almost all Bi minerals in each main-stage mineralization. Quartz-vein ores from Stages 2 and 3 have high Bi concentrations (up to 7332 ppm) and show a positive correlation between Bi and Au, with Bi/Au ratios > 10. These textural and geochemical associations, together with the occurrence of numerous droplet-like blebs and small inclusion trails of native bismuth and Bi-tellurides with native gold, maldonite, or jonassonite, suggest that Bi-rich melts may have formed from the hydrothermal fluids of Stages 2 and 3, and acted as an Au scavenger in a complex Bi-Au-Pb-Ag-Te system. Hence, the intimate association of Bi and Au at Wulong is the result of Au enrichment via the liquid bismuth collector mechanism. Unlike Wulong, however, other deposits in the NCC, such as Yangzhaiyu (Xiaoqinling district), Guilaizhuang (Jiaodong district) and Dongping (Jidong district), are characterized by low Bi concentrations, and are much richer in Te than Bi, so these systems could not generate low-melting point Bi-rich polymetallic melts. The low-sulfur Bi-Au-Pb-Ag-Te association at Wulong is consistent with that observed in reduced intrusion-related gold systems elsewhere and suggests that hydrothermal fluids may have been derived from the co-located Early Cretaceous diorite-granite porphyry dyke swarm.

Keywords Bismuth minerals · Liquid bismuth collector · Chemical fluctuations · Wulong gold deposit · North China Craton

Introduction

Understanding the processes controlling metal precipitation and accumulation is fundamental to the study of gold deposit formation. The North China Craton (NCC) is the most

---

Editorial handling: S. Hagemann

✉ Ping Shen
pshen@mail.iggcas.ac.cn

[1] Key Laboratory of Mineral Resources, Institute of Geology and Geophysics, Chinese Academy of Sciences, Beijing 100029, China

[2] College of Earth and Planetary Sciences, University of Chinese Academy of Sciences, Beijing 100049, China

[3] Innovation Academy of Earth Science, Chinese Academy of Sciences, Beijing 100029, China

[4] State Key Laboratory of Lithospheric Evolution, Institute of Geology and Geophysics, Chinese Academy of Sciences, Beijing 100029, China

[5] School of Earth, Atmosphere and Environment, Monash University, Clayton, VIC 3800, Australia

important Au-producing region in China. It hosts numerous large to world-class Au deposits in several districts, such as the Jiaodong district in the eastern NCC and the Xiaoqinling district in the southern NCC (ESM 1 Fig. S1a); altogether these districts host Au reserves of ~ 4,000 to 5,000 t (Goldfarb and Santosh 2014; Zhu et al. 2015).

Gold deposits in the NCC have been divided into "altered-wallrock" and "quartz-vein" types (Zhu et al. 2015; Fan et al. 2016), and many contain trace amounts of tellurides and/or bismuth minerals (Gu et al. 2003; Bi et al. 2011, 2016; Zhou et al. 2011; Li et al. 2006, 2012a, b; Xu et al. 2014; Yang et al. 2016b; Feng et al. 2019, 2020). The Wulong gold deposit is an example of the quartz vein type, located in the northeastern margin of the NCC (Fig. 1; Feng et al. 2020). Generally, the hydrothermal fluids in both types of gold deposits share similar chemical and physical properties, including temperature (200–410 °C), salinities (< 15 wt% NaCl eq.), and enrichment in CO_2 (Zhu et al. 2015; Fan et al. 2016). Available geochronological data suggest that these gold deposits formed mostly over a short period in the Early Cretaceous (130–120 Ma; Zhu et al. 2015). Several processes have been suggested to trigger Au enrichment from hydrothermal fluids to form economic Au accumulation in this region. Visible gold in the quartz-vein type deposits may have precipitated upon phase separation (boiling) of the ore-forming fluid in response to pressure and temperature fluctuations (Jiang et al. 1999; Jiang 2000; Zhou et al. 2014, 2015; Fan et al. 2016; Guo et al. 2017, 2020), whereas intense fluid-rock interaction may have been important to the formation of altered-wallrock type gold deposits (Fan et al. 2003, 2016; Yang et al. 2015, 2016a, 2017; Guo et al. 2017). Other gold enrichment mechanisms invoked in the NCC are: (1) partitioning of invisible Au into As-bearing pyrite (Mills et al. 2015; Feng et al. 2018; Li et al. 2018); (2) accumulation of Au onto the surfaces of pre-deposited As-rich pyrite (Mills et al. 2015); and (3) Au–Ag-Te-rich melt scavenging Au from fluids into As-free pyrite in Au–Ag telluride-bearing mineralized systems (Cook et al. 2009; Jian et al. 2021). Very recently, a potential role for bismuth in Au enrichment in the NCC has been reported (Wei et al. 2021).

Bismuth is one of the most important low melting chalcophile elements (LMCE; Frost et al. 2002), because it is relatively abundant and has a low melting temperature of 271 °C (at 1 bar, slightly lower at higher pressures; Ponyatovskii 1960). In systems involving Au and/or Te, the melting temperature can be even lower (Fig. 2). For example, the native bismuth + maldonite assemblage melts at 241 °C at the eutectic composition in the Au-Bi system (87.4 wt % Bi and 12.6 wt % Au; Okamoto and Massalski 1983), and the eutectic in the Au-Bi-Te system is located at 235 °C. Once precipitated from hydrothermal fluids as a liquid, droplets of Bi melt can efficiently scavenge tens of wt. % Au from coexisting fluid, even if that fluid is Au undersaturated (Douglas et al. 2000; Tooth et al. 2008, 2011). This is the liquid bismuth collector model of Douglas et al. (2000), which is well supported by thermodynamic modeling and experimental studies (Tooth et al. 2008, 2011). Since Douglas et al. (2000), it has been suggested that the liquid bismuth collector mechanism played a role in the formation of several hydrothermal gold deposits (e.g., Romanian gold deposits, Ciobanu et al. 2003, 2006; Cook and Ciobanu 2004; modern volcanic-hosted massive sulfide at Escanaba Trough, Southern Gorda Ridge, Törmänen and Koski 2005; Viceroy orogenic gold deposit in Zimbabwe, Oberthür and Weiser 2008; Maldon gold deposit, Ciobanu et al. 2010; Stormont Bi-Au skarn prospect in Australia, Cockerton and Tomkins 2012; Geodo skarn gold deposit in South Korea, Kim et al. 2012; iron oxide-dominated NICO Au–Co-Bi (± Cu ± W) deposit, Canada, Acosta-Góngora et al. 2015; skarn ores from the Beiya Fe-Cu-Au deposit, China, Zhou et al. 2017), where sulfur fugacity was sufficiently low to stabilize native bismuth rather than bismuthinite (Tooth et al. 2013). Gold scavenging by Bi-rich melts accounts for the close correlation of Bi and Au concentrations found in these deposits. In addition, bismuth minerals can be valuable tracers of fluid evolution because they are sensitive to physical–chemical fluctuations (Cook and Ciobanu 2004; Cepedal et al. 2006; Ciobanu et al. 2010; Voronin and Osadchii 2013; Zhou et al. 2016, 2018).

The Wulong gold deposit, located in the Liaodong Peninsula, northeastern NCC (Fig. 1a; ESM 1 Fig. S1), is an Early Cretaceous Au deposit that is enriched in Bi and Te. At Wulong, Bi- and Te-bearing minerals were reported in the auriferous quartz veins as early as the 1980s (Li et al. 1987). Zhao et al. (1994) were the first to describe the association between Au mineralization and native bismuth, bismuthinite and galenobismutite, but subsequent studies have largely ignored this association. Wei et al. (2021), however, described a similar association of native gold with native bismuth and Bi-Te-S minerals. They suggested that Au deposition occurred mainly during one stage, during which Bi-(Te)-rich melts may act as Au scavengers. However, further petrographic evidence is needed to support this model. In addition, multi-stage gold mineralization and Bi mineral formation have been documented at Wulong (Wei et al. 2001), raising the possibility that different Au scavenging mechanisms formed different stages of gold mineralization at Wulong.

This paper presents new mineralogical data for the Wulong gold deposit, including detailed petrographic observations on the phase relationships among Au-Bi-Te mineral assemblages and in situ major and trace element data. The results provide new insights into the evolving chemistry and physicochemical conditions that controlled Au accumulation. In particular, our petrographic and geochemical evidence imply that multi-stage scavenging of Au by Bi-rich

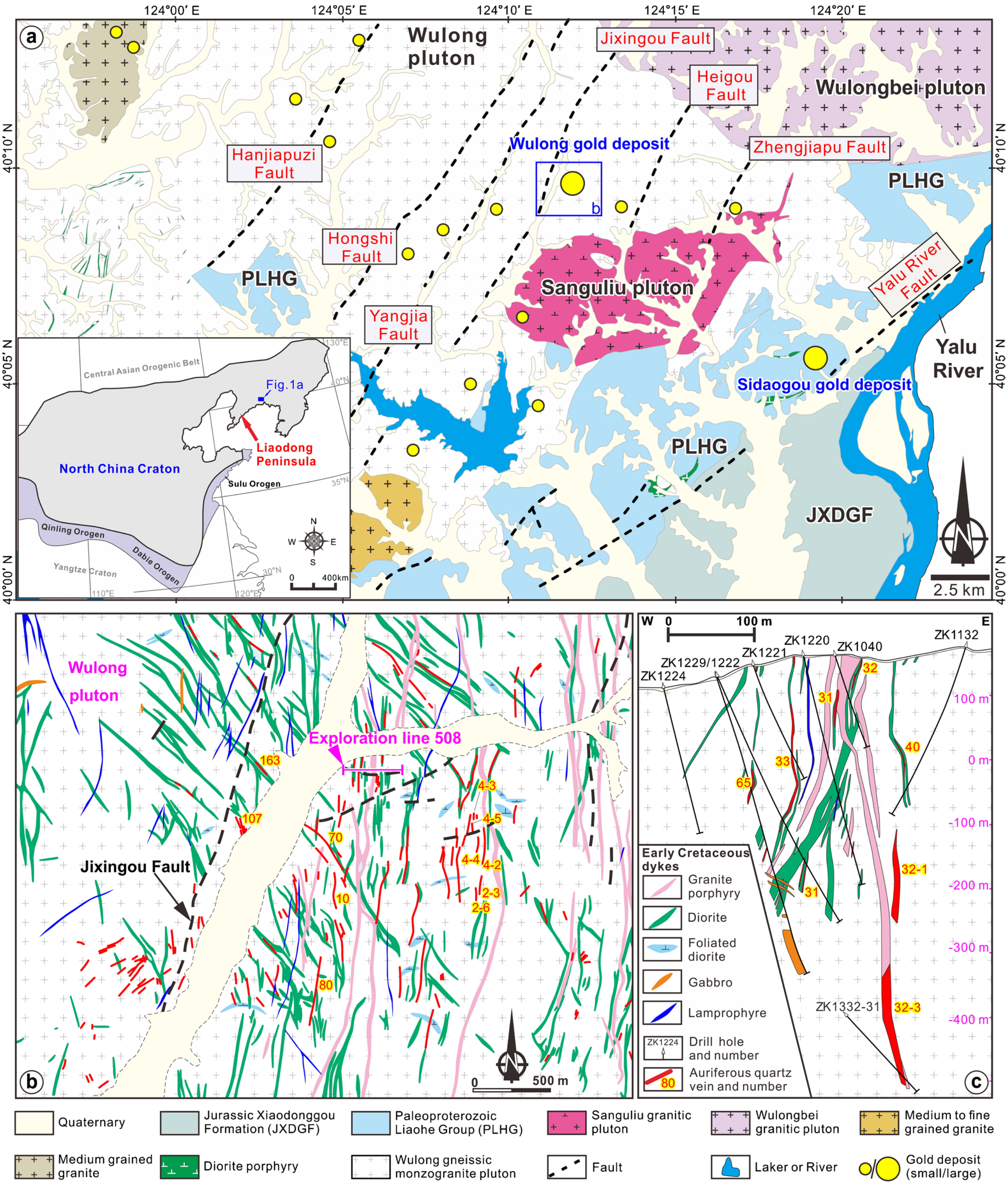

Fig. 1 **a** Geological map of the Wulong gold orefield (modified after Feng et al. 2020). The inset (modified after Zhu et al. 2015) shows the location of the Wulong gold orefield within the North China Craton. **b** Schematic geological map of the Wulong gold deposit (modified after Feng et al. 2020). **c** Simplified cross section of prospecting line 508 (modified after Yu et al. 2018)

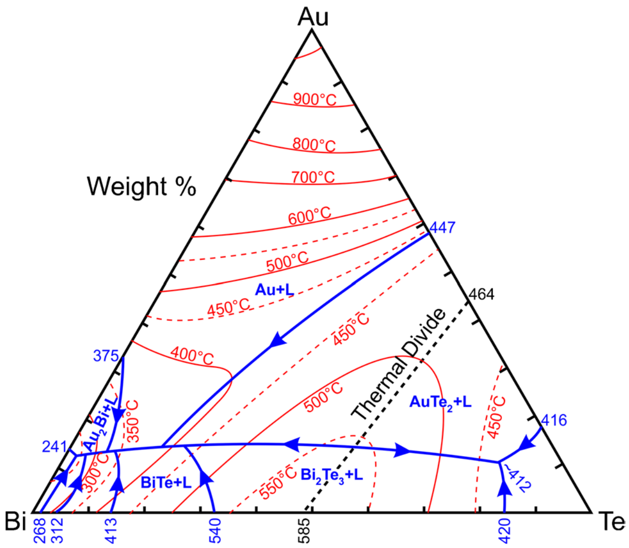

Fig. 2 Schematic Au-Bi-Te ternary phase diagram derived from the three binary systems (Au-Bi binary, after Okamoto and Massalski 1983; Au-Te binary, after Okamoto and Massalski 1986; Bi-Te binary, after Okamoto and Tanner 1990)

polymetallic melt was responsible for gold enrichment in auriferous quartz veins at Wulong. These observations emphasize the importance of studying Bi mineral paragenesis to unraveling the ore-forming processes of hydrothermal Au deposits globally.

Geological setting

The Wulong gold deposit is located in the Wulong Au orefield, eastern Liaodong Peninsula, at the northeastern margin of the NCC (Fig. 1a; ESM 1 Fig. S1a). The Precambrian basement in the Liaodong Peninsula includes Archean tonalite-trondhjemite-granodiorite (TTG) gneisses and the Paleoproterozoic Liaohe Group, which is dominated by metamorphic sedimentary and bimodal volcanic rocks (Liu et al. 1992; Lu et al. 2004; Li et al. 2005; ESM 1 Fig. S1b). This basement was intruded by widespread Mesozoic felsic to intermediate magmas, produced by the destruction of the NCC and related lithospheric thinning (Yang et al. 2008; Zhu et al. 2011; Wu et al. 2019), predominantly emplaced in the Late Jurassic (180–153 Ma) and Early Cretaceous (131–110 Ma), with minor Triassic magmatism (230–210 Ma) (Wu et al. 2005a, b; Yang et al. 2007a, b). These rocks have a wide range of compositions, including nepheline syenite, syenite, tonalite, diorite, granodiorite, monzogranite, and syenogranite (ESM 1 Fig. S1b; Wu et al. 2005a, b; Yang et al. 2007a, b, 2012).

The Wulong orefield, at the eastern margin of the Liaodong Peninsula, is underlain by the Paleoproterozoic Liaohe Group and Jurassic Xiaodonggou Formation, both of which are only exposed to a limited extent (Fig. 1a). The metamorphic rocks of the Liaohe Group are mainly distributed west of the Yalu River Fault and are extensively intruded by Late Mesozoic granite (Fig. 1a). The Xiaodonggou Formation occurs east of Yalu River Fault and comprises siltstone, sandstone, tuffaceous shale, conglomerate, and marl (Fig. 1a). Structurally, the Wulong orefield is dominated by approximately parallel and regularly spaced NNE-trending faults, considered to be subsidiary to the NE-trending Yalu River Fault. These NNE-trending faults extend for several kilometers and dip 40°–60° to the west (Zhang 2002), and are represented by the Zhengjiapu, Heigou, Jixingou, Yangjia, Hongshi and Hanjiapuzi Faults from east to west (Fig. 1a). The major Yalu River Fault is ca. 700 km long and dips ca. 70° NW, and was initiated as a sinistral strike-slip fault zone between 146 and 131 Ma (Zhang et al. 2018).

The widespread igneous rocks in the Wulong orefield are dominated by the Late Jurassic Wulong two-mica monzogranite (163–155 Ma), Early Cretaceous Wulongbei porphyritic granite (127–125 Ma) and Sanguliu pluton (131–120 Ma) (Fig. 1a), comprising a central monzogranite and an encompassing granodiorite (Wu et al. 2005a, b; Meng et al. 2013; Gu et al. 2018; Yang et al. 2018). These rocks are intruded by numerous mafic to felsic dykes, including gabbro, lamprophyre, diorite, granite, and granitic pegmatite from 126 to 113 Ma (Fig. 1b; Zhang 2002; Xiao et al. 2018; Liu et al. 2019; Zhang et al. 2020). The orientation of these dykes parallels the Au-bearing quartz veins at Wulong (Fig. 1b).

Geology of the Wulong gold deposit

The Wulong auriferous quartz veins are located in an area of widespread Jurassic Wulong monzogranite with numerous crosscutting mafic to felsic dykes (Fig. 1b, c). The granite porphyry is consistently truncated by auriferous quartz veins (Fig. 1c), whereas the lamprophyre and gabbro dykes crosscut the auriferous quartz veins (Fig. 1b). In most cases, the fine-grained diorite dykes and the auriferous veins occupy the same fracture systems (Fig. 1b), where some fine-grained diorite dykes are crosscut by auriferous veins, and others have sharp contacts and no cross-cutting relationships, suggesting that the latter are broadly contemporaneous with the Au mineralization (Zhang 2002; Zhang et al. 2020). Several studies have indicated that these mafic to felsic dykes formed in the Early Cretaceous on the basis of zircon U–Pb ages between 126 ± 1 Ma and 115 ± 2 Ma (Zhang 2002; Liu et al. 2019; Zhang et al. 2020). Structurally, the distribution of dykes and Au-bearing quartz veins was controlled by a conjugate set of NW- and NS-oriented (dominant) faults and NE- and EW-oriented (less abundant) faults (Fig. 1b). The nearly

NS- and NW-oriented fault set was produced during the sinistral shearing along the Jixingou Fault (Wang et al. 2018).

The quartz vein orebodies

The Wulong gold deposit, discovered in 1939, consists of more than 380 auriferous quartz veins with a total proven reserve of more than 80 t Au (average grade of 5.35 g/t; Wang et al. 2018). These veins extend vertically up to 750 m, and their lengths and widths vary from ~ 25 to ~ 1230 m and ~ 0.1 to ~ 20 m, respectively. Important auriferous quartz veins include the No. 163, No. 80, No. 2–3, No. 4–2, No. 4–3, No. 32, No. 32–1, No. 65, and No. 107 lodes (Fig. 1b, c). No. 163 lode, with an average grade of 6.3 g/t Au, is the largest Au vein, and strikes northwest and dips toward southwest at an angle of 65° to 70° (Yu et al. 2018). This vein is ca. 1231 m long and has a width of ~ 0.5 to ~ 11.6 m, and extends more than 280 m vertically (Yu et al. 2018). No. 80 lode is the second largest Au vein with an average grade of 13.1 g/t, striking NNE and dipping 80°E. It is over 430 m in length and ~ 0.3 to ~ 2.5 m in width, and extends from a depth of ~ 360 to ~ 597 m (Yu et al. 2018).

Four stages of formation of the auriferous quartz veins have been established in this study on the basis of crosscutting relationships amongst the veins and veinlets, as well as from paragenetic, mineral-chemical, and textural observations by optical microscope, SEM and EPMA analyses. These stages consist of barren quartz ± pyrite (Stage 1), gold-pyrite-quartz (Stage 2), gold-polymetallic sulfide-quartz (Stage 3), and quartz-calcite (Stage 4) (Fig. 3a-d and ESM 1 Figs. S2, S3).

Stage 1, during which the main part of the quartz veins formed, is dominated by milky to clear quartz, locally with rare scheelite, and disseminated pyrite that commonly forms coarse, euhedral grains with cubic habit (Fig. 3a and ESM 1 Fig. S2a, c). Stage 2 is characterized by gold-quartz-pyrite veins, and pyrite stringers crosscutting the Stage 1 vein (Fig. 3a, b and ESM 1 Fig. S2a, b, d). Mineral assemblages mainly consist of pyrite-quartz (clear to gray)-chlorite ± scheelite ± electrum (Fig. 3a, b, f; ESM 1 Fig. S2a, b, d). Other sulfides, such as arsenopyrite, pyrrhotite and chalcopyrite, are rare (Fig. 3e). Locally, minor rutile and apatite can also be observed. Stage 3 is characterized by gold-polymetallic sulfide-quartz veins and stockwork veinlets (Fig. 3b and ESM 1 Fig. S2c, d), as well as thin sheeted veins (Fig. 3c), in which sulfides consist of pyrrhotite-pyrite-chalcopyrite ± galena ± sphalerite (Fig. 3b, g and ESM 1 Fig. S2c, d). Sulfides are accompanied by clear to gray quartz and minor scheelite (Fig. 3h). Importantly, there are abundant Bi minerals and tellurides in vein stages 2 and 3, with twenty minor minerals identified (see details below). Stage 4 is defined by a barren quartz-calcite assemblage, which is not common at Wulong (Fig. 3d). During this stage, the calcite formed coarse crystals in fractures within the proximal alteration zones or auriferous quartz veins.

Hydrothermal alteration

The immediate wall rocks, consisting of monzogranite, fine-grained diorite, and granite porphyry at Wulong, have been subjected to widespread hydrothermal alteration, with the most intense alteration occurring in and around the mineralized quartz veins. Alteration halos are generally several meters to tens of meters in width (Yu et al. 2018). The main alteration minerals are quartz, sericite, chlorite, biotite, and calcite, and varies with the nature of the host rocks (Zeng et al. 2019), that is, quartz ± sericite ± chlorite alteration in the Wulong monzogranite, quartz-sericite alteration in granite porphyry, and quartz-biotite-chlorite alteration in fine-grained diorite dykes (Zhang and Yang 1988; Zeng et al. 2019). Sericite, the most abundant alteration product following quartz, formed via replacement of host-rock plagioclase, whereas hydrothermal biotite formed via replacement of amphibole in fine-grained diorite dykes. These alteration facies were crosscut by an assemblage of calcite and quartz, which is seen as veins and veinlets (Stage 4).

Sample preparation and analytical method

More than 150 samples, collected from seven productive auriferous quartz veins from the Wulong underground mine at different mine levels (–479 to –636 m), were studied. Polished thin sections were used for petrographic observation by optical microscopy. Representative sections rich in Bi minerals were selected for further petrographic and geochemical studies. Mineral textures and semi-quantitative chemical compositions were investigated in back-scattered electron (BSE) mode using a LEO 1450VP Scanning Electron Microscope (SEM) coupled with an INCA ENERGY-300 Energy Dispersive X-ray Spectrometer (EDS). Bismuth mineral and chlorite compositions were determined by a JEOL JXA-8100 electron probe micro-analyzer (EPMA). Instrumental conditions, analyzed X-ray lines, background positions, counting times, analytical standards, average minimum detection limits, and analytical results are given in the ESM 1. All analyses were performed at the Institute of Geology and Geophysics, Chinese Academy of Sciences (IGGCAS), Beijing, China.

Bismuth minerals and gold mineralization

A large number of Bi minerals have been recognized in Stages 2 and 3, including native bismuth; bismuthinite; the Bi-tellurides hedleyite[Bi_7Te_3]; unnamed Bi_5Te_3, and unnamed

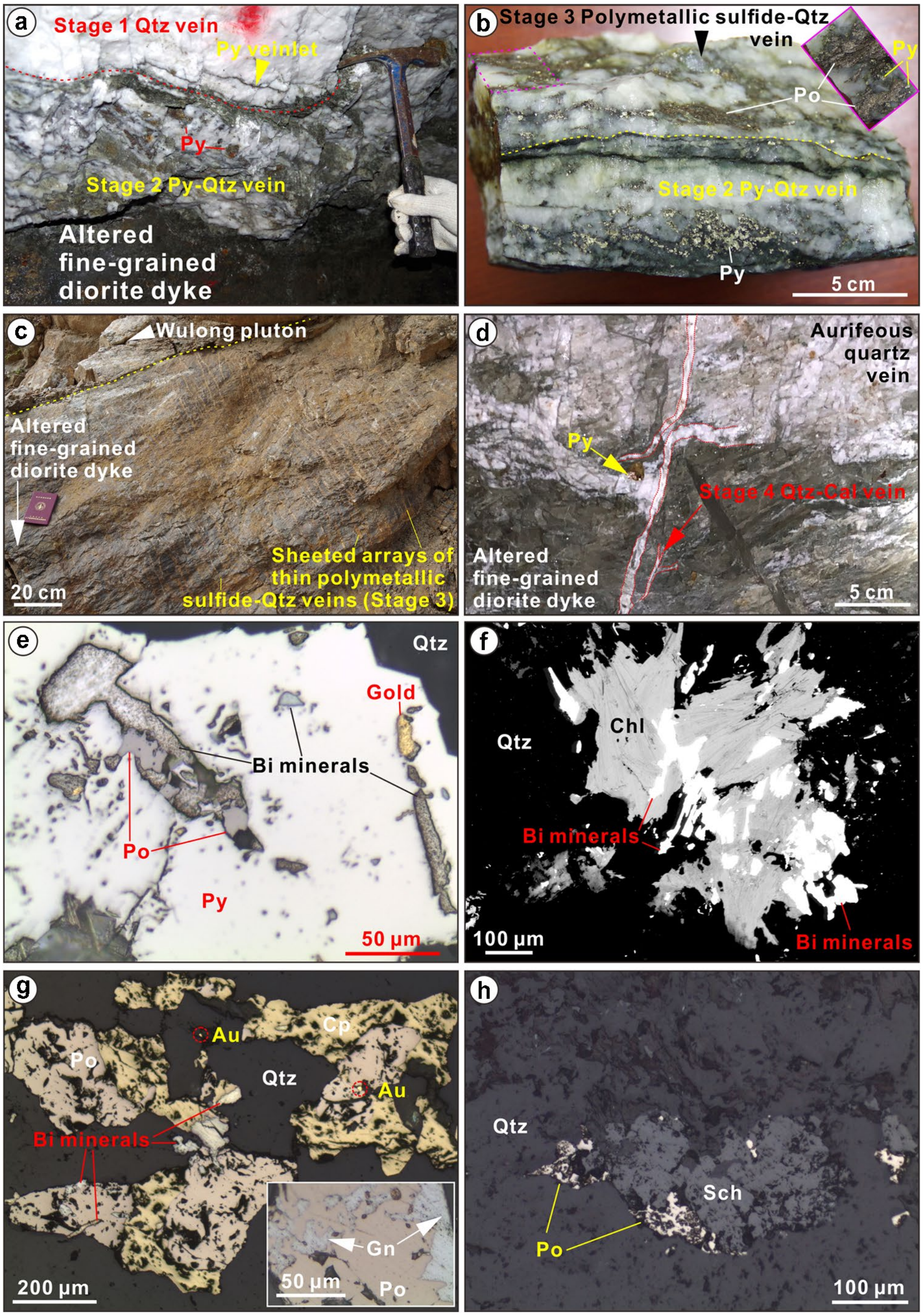

Fig. 3 Photographs (**a**-**d**), reflected-light photomicrographs (**e**, **g**, **h**), and BSE image (**f**) showing different stage quartz veins and associated ore-related mineral assemblages at the Wulong gold deposit. **a** Stage 2 pyrite-quartz vein overprints the Stage 1 barren milk quartz vein. **b** Stage 2 pyrite-quartz vein cut by a Stage 3 polymetallic sulfide-quartz vein that is dominated by pyrrhotite and minor pyrite (inset image). **c** Exposure of sheeted array of thin, low-grade polymetallic sulfide-quartz veins in fine-grained diorite dyke with intensive biotite alteration. Generally, these veins contain accessory scheelite and trace amounts of Bi minerals. **d** Stage 4 quartz-calcite vein cut through the early auriferous quartz vein. **e** Intergrowth of Bi minerals, pyrrhotite, and gold in a coarse, subhedral pyrite crystal in a Stage 2 quartz vein. **f** Bi minerals coexisting with chlorite in a Stage 2 quartz-pyrite vein. **g** Intergrowth of pyrrhotite, chalcopyrite and Bi mineral patches in a Stage 3 veins, showing native gold inclusions in pyrrhotite and quartz. The inset image shows the replacement of pyrrhotite by galena. **h** Scheelite intergrown with pyrrhotite in Stage 3 sheeted thin veins. Abbreviations: Au = native gold, Cal = calcite, Chl = chlorite, Cp = chalcopyrite, Gn = galena, Po = pyrrhotite, Py = pyrite, Qtz = quartz, Sch = scheelite

Bi_8Te_3; the Bi-sulfotellurides (tetradymite [Bi_2Te_2S], joséite-A [Bi_4TeS_2], joséite-B [Bi_4Te_2S] and ingodite [Bi_2TeS]); an unnamed Bi-Pb-sulfotelluride $(Bi,Pb)_3(Te,S)_4$; the Bi-Pb sulfosalts (galenobismutite [$PbBi_2S_4$] and cosalite [$Pb_2Bi_2S_5$]); the Bi-Ag sulfosalt (matildite [$AgBiS_2$]); the Bi-Pb-Ag sulfosalts (vikingite [$Ag_5Pb_8Bi_{13}S_{30}$], eskimoite [$Ag_7Pb_{10}Bi_{15}S_{36}$], lillianite-gustavite series [$Pb_{3-2x}Ag_xBi_{2+x}S_6$ – $AgPbBi_3S_6$], and galen-matildite series [PbS – $AgBiS_2$]); and the Bi-Au minerals (maldonite [Au_2Bi] and jonassonite [$AuBi_5S_4$]). Among them, Bi-Pb sulfosalts, Bi-Ag sulfosalts, and Bi-Pb-Ag sulfosalts only formed in Stage 2 (ESM 1 Fig. S3). Most of these Bi minerals are commonly present as small droplets, and composite blebs or patches that include two or more phases (Figs. 4 and 5). The patches are lens-shaped, or elongate blades, ranging in lengths from several tens to hundreds of μm (Fig. 4a, b, e). The small droplets and blebs are commonly a few and several tens of microns in size, respectively (Figs. 4c, d, f and 5). In most cases, each single bleb or patch displays both curved and angular edges (Figs. 4a, d, f, and 5h).

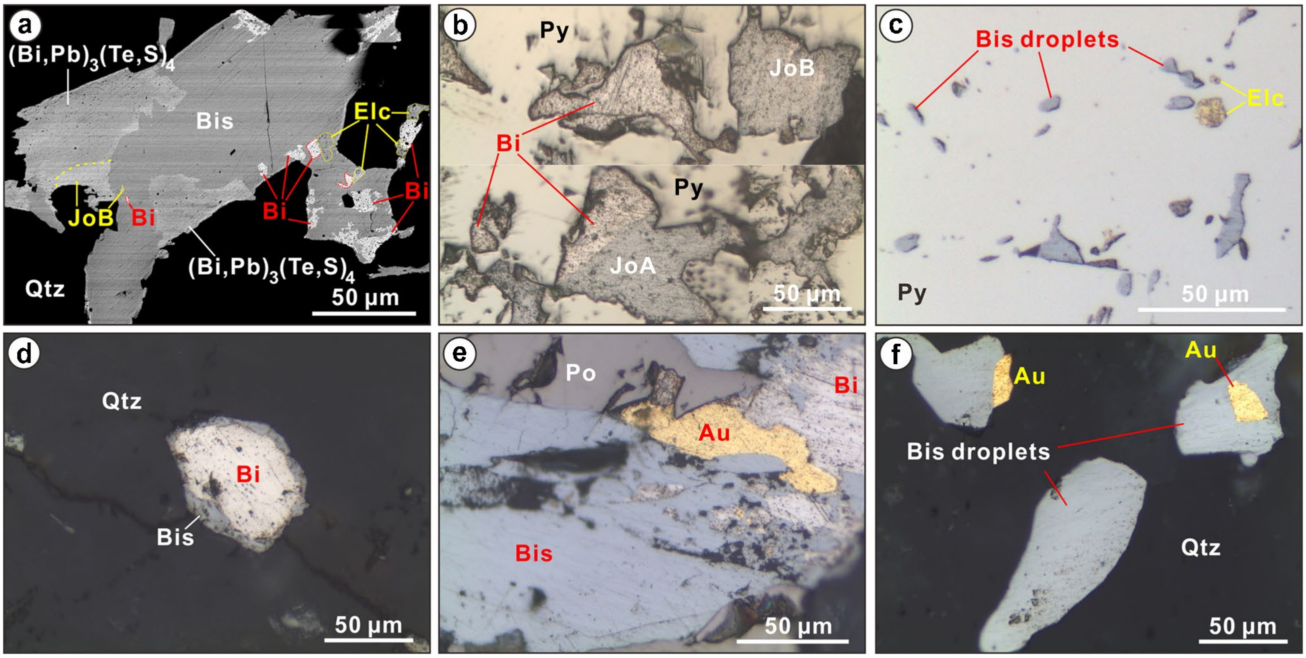

Fig. 4 Back-scattered-electron (BSE) image (**a**) and reflected-light photomicrographs (**b**-**l**) showing the occurrence of native bismuth and bismuthinite in the Wulong gold deposit. **a** A large patch of bismuthinite in Stage 2 quartz, hosting small inclusions of joséite-B and native bismuth, has been replaced by the unnamed (Bi,Pb)$_3$(Te,S)$_4$ at its margin. Note that electrum grains can also be present in this bismuthinite and its margin with native bismuth as composite blebs. **b** Composite patches of native bismuth with joséite-B, and joséite-A enclosed in Stage 2 pyrite. **c** Small bismuthinite droplets and nearby electrum inclusions in Stage 2 pyrite. **d** A large droplet of native bismuth rimmed by bismuthinite in quartz from Stage 3. **e** Stage 3 bismuthinite replacing pyrrhotite and native bismuth that are in contact with native gold. **f** Bismuthinite droplets intergrown with native gold in Stage 3 quartz. Abbreviations: Au = native gold, Bi = native bismuth, Bis = bismuthinite, Elc = electrum, JoA = joséite-A, JoB = joséite-B, Po = pyrrhotite, Py = pyrite, Qtz = quartz

Native bismuth and bismuthinite

Native bismuth and bismuthinite are identified in Stages 2 and 3. In Stage 2, native bismuth is present as single inclusions with sub-rounded to elongate habit in quartz and pyrite, or occurs together with bismuthinite, joséite-A, joséite-B, and/or electrum in composite patches (Fig. 4a, b and ESM 1 Fig. S4a). In the latter, bismuthinite has replaced native bismuth, joséite-A, and joséite-B (Fig. 4a and ESM 1 Fig. S4a). Bismuthinite also occurs as coarser patches with ingodite (ESM 1 Fig. S4b), and as small single blebs clustered within pyrite (Fig. 4c). In Stage 3, relatively large native bismuth blebs (50 to 200 µm) are located at the margins of pyrrhotite, and in quartz, and can be partly rimmed by bismuthinite and galena (Fig. 4d and ESM 1 Fig. S4c). Stage 3 native bismuth also occurs as inclusions in bismuthinite, joséite-A, and joséite-B in single or composite patches. In some cases, native bismuth grains are intergrown with native gold and the unnamed Bi_5Te_3 phase. Bismuthinite is commonly present as large patches replacing pyrrhotite and native bismuth (Fig. 4e), and as small single blebs enveloped by pyrite and quartz (Fig. 4f and ESM 1 Fig. S4d), and can host native gold grains (Fig. 4f).

Importantly, in both Stage 2 and 3, the smallest native bismuth and bismuthinite droplets (< 5 µm) appear as inclusion trails adjacent to the large Bi mineral patches, pyrite, and pyrrhotite (Fig. 5a-h and ESM 1 Fig. S5a-e). In the trails, bismuthinite can form two-component droplets with hedleyite or gold (Fig. 5b, e), and native bismuth can coexist with hedleyite and maldonite in three-component droplets in Stage 2 (Fig. 5d). In Stage 3, however, native bismuth in the trails can appear in four-component droplets, together with gold, hedleyite and the unnamed Bi_8Te_3 phase (Fig. 5h).

All bismuthinite grains are distinctly Pb-rich (ESM 1 Table S1). In Stage 2, bismuthinite contains 1.03 to 1.28 wt % Pb, and variable amounts of Sb (0.00 to 0.18 wt %), Cu (0.09 to 0.27 wt %), and Te (0.00 to 1.54 wt %). Bismuthinite in Stage 3 contains high Pb (up to 1.34 wt %), Sb (up to 0.44 wt %), Cu (up to 0.33 wt %), and Te (up to 0.22 wt %).

Bi-tellurides

Bi-tellurides include hedleyite, unnamed Bi_5Te_3, and unnamed Bi_8Te_3; the latter two phases were only identified in Stage 3. In Stage 2, hedleyite is one of the Bi minerals occurring as droplets in the inclusion trails

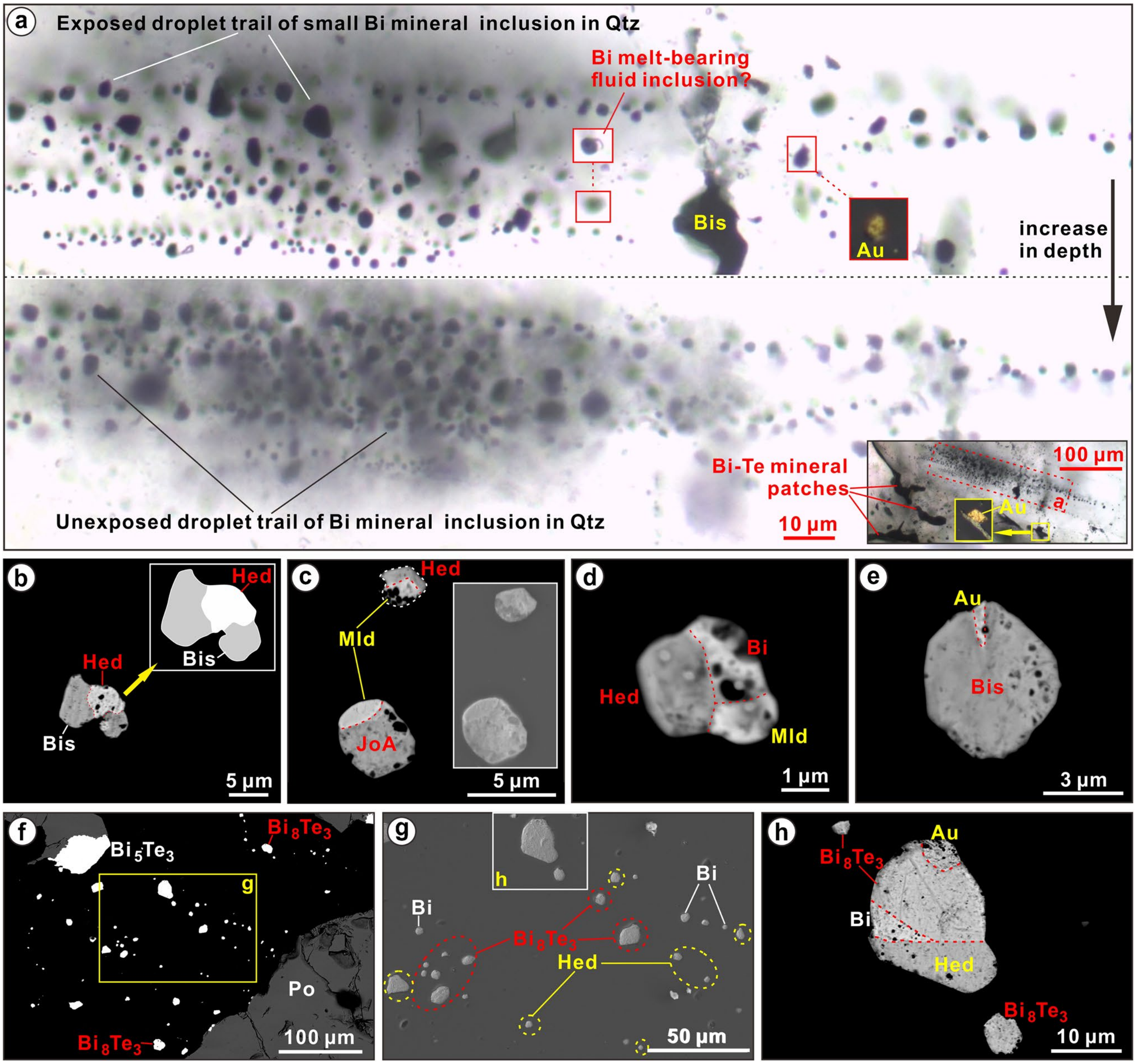

Fig. 5 Photomicrographs of droplet trails of small Bi mineral inclusions in Stages 2 (**a**-**e**) and 3 (**f**–**h**) quartz in the Wulong gold deposit. **a** Small Bi mineral inclusion trails are not only exposed in the polished surface of quartz, but also located at the depth of quartz crystal. The quartz crystal is located nearby several large Bi-Te mineral patches. In the trails, rare gold and Bi melt-bearing fluid inclusions (reflected-light) are also present. **b** Bismuthinite intergrown with hedleyite in a droplet. **c** Spherical two-component droplets of maldonite with hedleyite, and joséite-A (Inset image, secondary electron image). **d** Intergrowth of native bismuth, maldonite and hedleyite in a spherical three-component droplet. Among them, triple-point junctions are present, indicating crystallization at equilibrium. **e** Native gold and bismuthinite in a two-component droplet. **f** Small Bi mineral inclusion trails nearby a patch of Bi_5Te_3 were found in quartz enveloped by pyrrhotite. **g** The trails mainly consist of spherical droplets of native bismuth, hedleyite, and unnamed Bi_8Te_3. **h** A four-component droplet hosting native bismuth, native gold, hedleyite, and unnamed Bi_8Te_3. **a**, polarized light; **b**-**f**, **h**, BSE image; **g**, Secondary electron image. Abbreviations: Au = native gold, Bi = native bismuth, Bis = bismuthinite, Hed = hedleyite, JoA = joséite-A, Mld = maldonite, Po = pyrrhotite, Py = pyrite, Qtz = quartz

(Fig. 5b-d), either as single droplets (ESM 1 Fig. S5d) or as composite blebs with maldonite, bismuthinite, or native bismuth (Fig. 5b-d). In Stage 3, hedleyite also occurs as small droplets in trails (Fig. 5g, h), and less commonly, as irregular inclusions in large patches of joséite-B (ESM 1 Fig. S6a). Hedleyite tends to be enriched in Bi and depleted in Te relative to its ideal composition (Fig. 6a); one Stage 3 grain has elevated Pb concentrations (0.71

wt %), and minor Sb (0.11 wt %), Se (0.14 wt %), and S (0.10 wt %) (ESM 1 Table S2).

The unnamed Bi_5Te_3 phase is closely intergrown with joséite-B as blebs enclosed in pyrrhotite, or as elongate patches with irregular partial replacement of pyrrhotite (ESM 1 Fig. S6b, c), or at pyrrhotite edges (Fig. 5f). This phase contains minor Pb (up to 0.40 wt %), Sb (up to 0.27 wt %), Se (up to 0.12 wt %), and S (up to 0.18 wt %) (ESM 1 Table S2).

The unnamed Bi_8Te_3 phase commonly occurs as small droplets in the trails of Bi mineral inclusions (Fig. 5g, h), locally in contact with native gold in composite droplets (Fig. 5h). Large two-component blebs of unnamed Bi_8Te_3 with native bismuth are also observed in galena (ESM 1 Fig. S6d). Unnamed Bi_8Te_3 contains 0.11–0.55 wt % Pb, 0.03–0.14 wt % Sb, and 0.13–0.29 wt % Se (ESM 1 Table S2).

Bi-sulfotellurides

Bi-sulfotellurides are abundant in the Wulong gold deposit, consisting of tetradymite, joséite-A, joséite-B, and ingodite (Fig. 7a-j). All occur in Stages 2 and 3 except tetradymite, which is only found in Stage 2. Representative EPMA data are listed in ESM 1 Table S3 and plotted in a ternary (Bi + Pb)-Te-(S + Se) diagram in Fig. 6a.

Tetradymite is a rare phase in the Stage 2 veins, occurring with joséite-B, and hessite in composite patches at the margins of pyrite (Fig. 7a). It has elevated Pb contents (0.92 to 1.57 wt %) (ESM 1 Table S3), indicating significant Pb substitution for Bi (Cook et al. 2007).

Joséite-A is another phase in the Stage 2 Bi mineral droplet trails (Fig. 5c and ESM 1 Fig. S5c, d), where it sometimes coexists with maldonite in composite droplets (Fig. 5c). Joséite-A also occurs in large patches within pyrite or at pyrite margins, in the form of isolated crystals or as intergrowths with native bismuth, bismuthinite, joséite-B, and electrum (Figs. 4b and 7c). Joséite-A in Stage 2 contains Pb (0.35 to 2.01 wt %) and Se (0.15 to 0.29 wt %) (ESM 1 Table S3). In Stage 3, joséite-A is relatively abundant and appears in large patches in contact with several minerals, including native bismuth, bismuthinite, joséite-B, pyrrhotite, chalcopyrite, and native gold (Fig. 7f). Rare droplets of Joséite-A are also observed in the Bi mineral inclusion trails. It is richer in Pb (0.38–4.68 wt %), and Au (0.00–0.73 wt %) compared to its Stage 2 counterpart (ESM 1 Table S3).

Stage 2 joséite-B is spatially associated with most of the Bi minerals, located in composite patches, in contact with native bismuth, hessite, ingodite, bismuthinite, Joséite-A, unnamed $(Bi,Pb)_3(Te,S)_4$, cosalite, galena-matildite series, lillianite-gustavite series, and electrum (Figs. 4b, 7a-d and 8d-e). It also

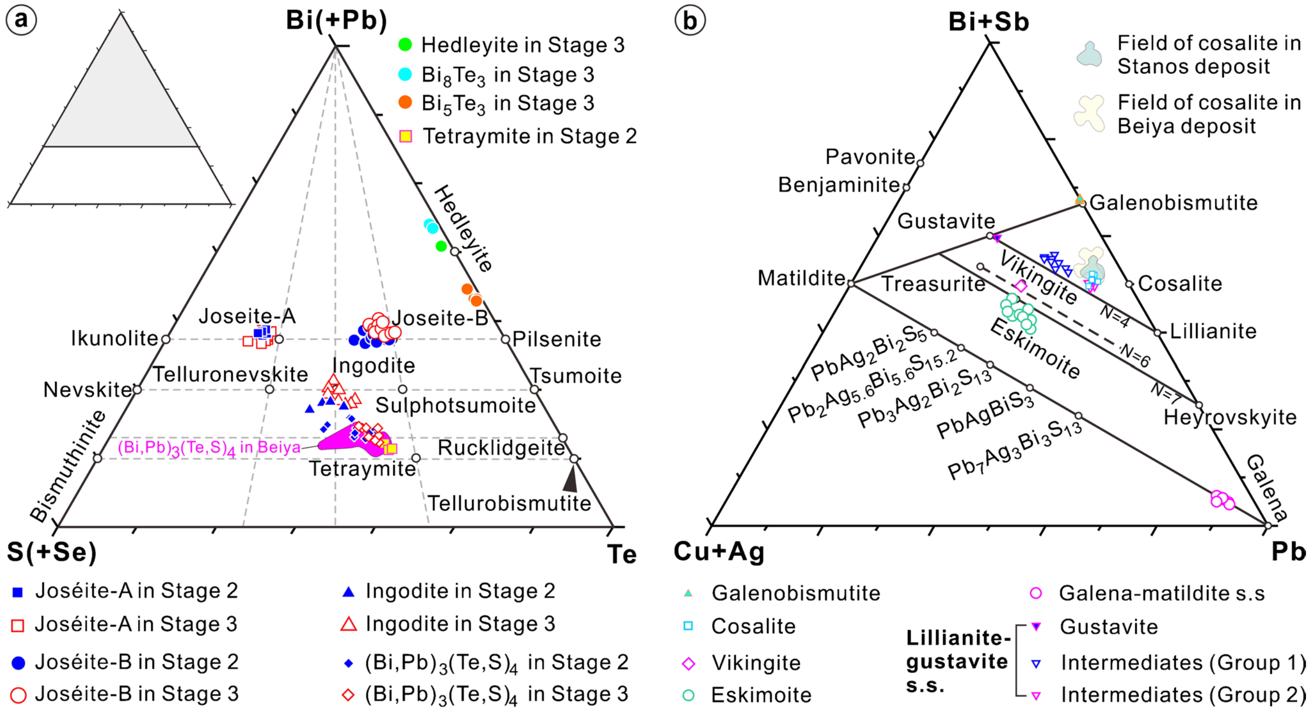

Fig. 6 **a** Ternary plot (Bi + Pb)-Te-(S + Se) of Bi-tellurides, Bi-sulfotellurides, and Bi-Pb sulfotellurides (the unnamed $(Bi,Pb)_3(Te,S)_4$) in the Wulong gold deposit (modified after Cook et al. 2007). **b** Ternary diagram of Bi-Pb and Bi-Pb-Ag sulfosalts in the Wulong gold deposit. Field of cosalite in the Stanos gold deposit, and of unnamed $(Bi,Pb)_3(Te,S)_4$ and cosalite from the Beiya Cu-Fe-Au deposit were sourced from Voudouris et al (2013) and Zhou et al (2016), respectively

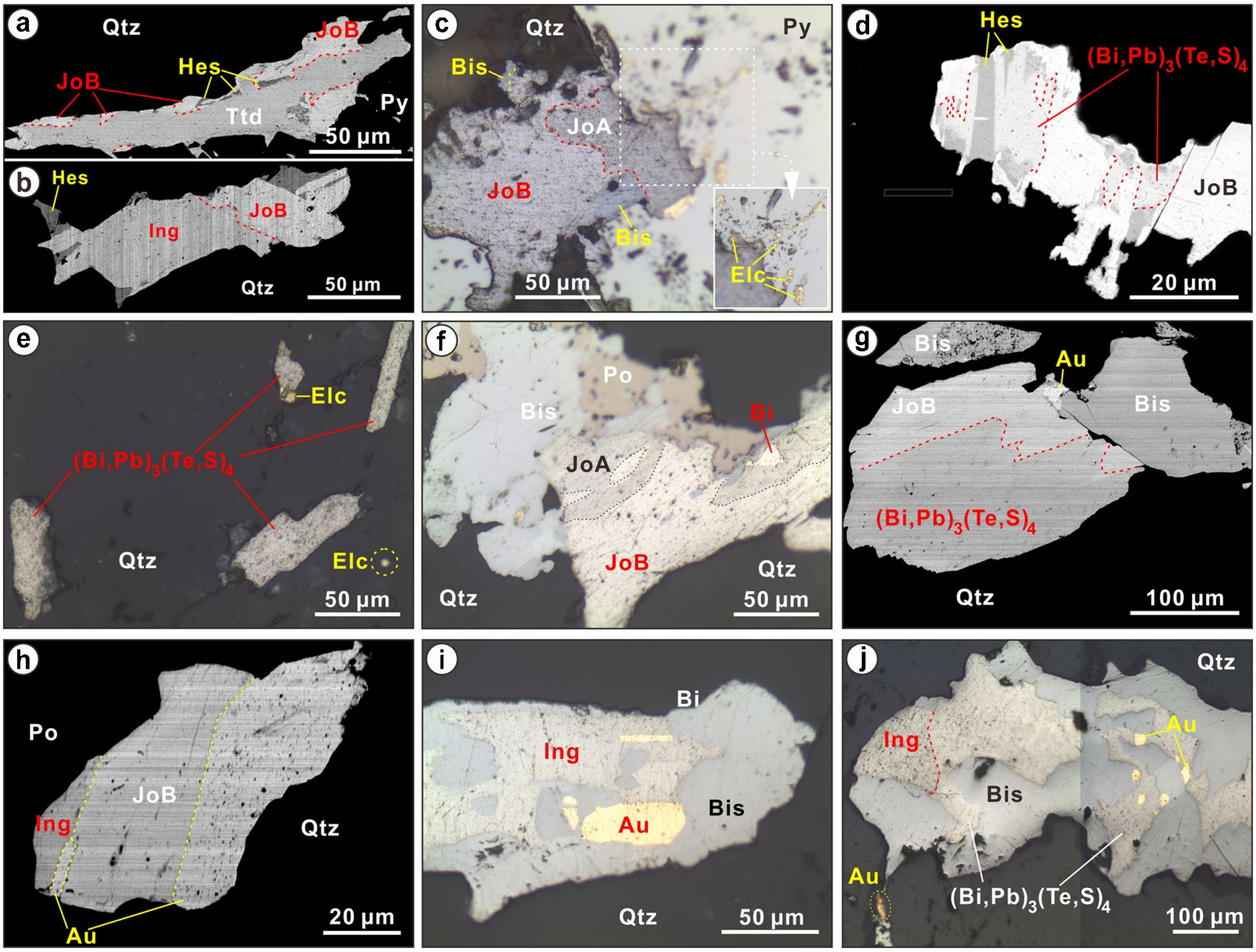

Fig. 7 Back-scattered-electron (BSE) images (**a**, **b**, **d**, **g** and **h**) and reflected-light photomicrographs (**c**, **e**, **f**, **i**, **j**) showing the occurrence and textures of Bi-sulfotellurides and Bi-Pb sulfotellurides in Stage 2 (**a**-**e**) and 3 (**f**-**j**) at the Wulong gold deposit. **a** A large patch of tetradymite containing hessite inclusions has been partly replaced by joséite-B at its margin. **b** A composite patch of ingodite, joséite-B, and hessite in quartz. **c** A composite patch of joséite-A, joséite-B, and bismuthinite and electrum in contact with pyrite. Electrum grains are also present as small inclusions in the nearby pyrite. **d** A large patch of joséite-B has been partly replaced by hessite and unnamed $(Bi,Pb)_3(Te,S)_4$. **e** Unnamed $(Bi,Pb)_3(Te,S)_4$ phase hosted in quartz. This phase coexists with electrum in the smallest grain. **f** A large patch of joséite-B and joséite-A partly replaced and rimmed by bismuthinite. Small native bismuth inclusions are present in joséite-A. **g** Intergrowth of the unnamed $(Bi,Pb)_3(Te,S)_4$, joséite-B, native gold, and bismuthinite from a large patch in quartz. **h** A composite bleb in contact with pyrrhotite composed by ingodite, joséite-B and native gold. **i** Ingodite hosting native gold inclusions has replaced the bismuthinite in a large patch. **j** Ingodite coexisting with the unnamed $(Bi,Pb)_3(Te,S)_4$, which has replaced bismuthinite. Seven native gold grains are present in this composite patch. Abbreviations: Au = native gold, Bi = native bismuth, Bis = bismuthinite, Elc = electrum, Hes = hessite, Ing = ingodite, JoA = joséite-A, JoB = joséite-B, Po = pyrrhotite, Py = pyrite, Qtz = quartz, Ttd = tetradymite

appears as isolated grains with irregular shapes in quartz and pyrite, and at pyrite margins. In Stage 3, joséite-B is found in patches together with native bismuth, native gold, joséite-A, bismuthinite, ingodite, unnamed Bi_5Te_3, and unnamed $(Bi,Pb)_3(Te,S)_4$ (Fig. 7f-h), as well as isolated crystals in quartz and pyrrhotite. Stage 2 joséite-B has variable Pb (0.15–1.10 wt %), Sb (0.00–0.20 wt %), Ag (0.00–0.38 wt %), Au (0.00–1.43 wt %), and Se (0.14–0.59 wt %); and Stage 3 joséite-B has similar contents of Pb (0.21–1.09 wt %), Sb (0.00–0.23 wt %), and Se (0.08–0.74 wt %), but slightly lower Ag (0.00–0.12 wt %) and Au (0.00–0.31 wt %) (ESM 1 Table S3).

Ingodite in Stage 2 occurs with bismuthinite or joséite-B in quartz, and with lillianite-gustavite series in pyrite (Figs. 7b and ESM 1 Fig. S4b). It contains high Pb (4.22 to 5.48 wt %), and variable amounts of Sb (0.01–0.17 wt %), Au (0.00–0.59 wt %), and Se (0.11–0.21 wt %) (ESM 1 Table S3). In Stage 3, ingodite is closely associated with bismuthinite, joséite-B, the unnamed $(Bi,Pb)_3(Te,S)_4$ phase, and native gold (Fig. 7h-j). This ingodite has lower Pb (0.66–2.57 wt %) than the Stage 2 counterpart, but similar Sb (0.02–0.22 wt %), Au (0.00–0.41 wt %), and Se (0.15–0.37 wt %) (ESM 1 Table S3).

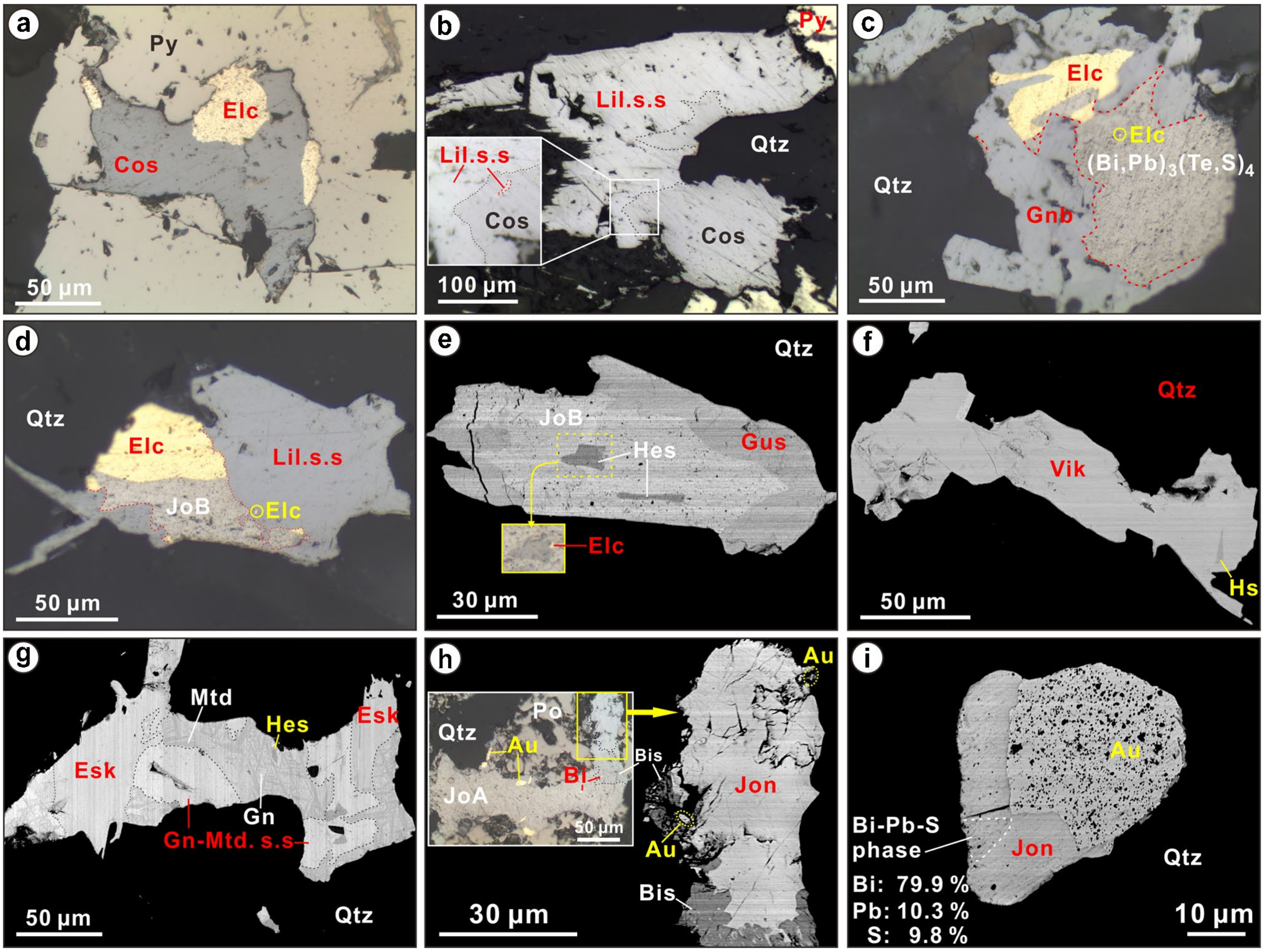

Fig. 8 Reflected-light photomicrographs (**a**-**d**), and back-scattered-electron (BSE) images (**e**-**i**) showing the occurrences and textures of Stage 2 Bi sulfosalts and Stage 3 jonassonite at the Wulong gold deposit. **a** A patch of cosalite containing electrum inclusion was enveloped by pyrite. **b** Lillianite-gustavite solid solutions (Group 1) partly replaced by cosalite in a large patch at pyrite margins. **c** A composite quartz-hosted bleb consisting of galenobismutite, unnamed $(Bi,Pb)_3(Te,S)_4$, and electrum. **d** Intergrowth of joséite-B and electrum, which both were enveloped by Lillianite-gustavite solid solutions (Group 2) in a large composite quartz-hosted patch. **e** Gustavite overgrown with joséite-B that contains small hessite and electrum (inset, reflected-light) inclusions in a bleb. **f** A patch of vikingite in quartz. **g** Galena-matildite solid solutions partly decomposed into matildite and galena, and replaced by eskimoite. **h** Jonassonite, joséite-B, bismuthinite, native bismuth, and native gold in a composite patch in contact with pyrrhotite. **i** Jonassonite, native gold and a Bi-Pb–S phase in a quartz-hosted bleb. Abbreviations: Au = native gold, Bi = native bismuth, Bis = bismuthinite, Elc = electrum, Esk = eskimoite, Cos = cosalite, Gn = galena, Gnb = galenobismutite, Gn-Mtd s. = galena-matildite solid solutions, Gus = gustavite, Hes = hessite, JoA = joséite-A, JoB = joséite-B, Jon = jonassonite, Lil s.s. = Lillianite-gustavite solid solutions, Mtd = matildite, Po = pyrrhotite, Py = pyrite, Qtz = quartz, Vik = vikingite

Bi-Pb-sulfotellurides

The only Bi-Pb-sulfotelluride recognized at Wulong is the unnamed $(Bi,Pb)_3(Te,S)_4$, which is common in Stages 2 and 3 (Fig. 6a). In Stage 2, the unnamed $(Bi,Pb)_3(Te,S)_4$ phase occurs in contact with many Bi minerals in composite patches, including joséite-B, cosalite, galenobismutite, bismuthinite, and lillianite-gustavite series (Figs. 7d and 8c). It is also spatially associated with hessite and electrum (Fig. 7d, e), and appears as isolated crystals with elongated habit in quartz (Fig. 7e). The analyzed phases have large variations in Pb (2.01 to 12.67 wt %), and Sb (0.02–0.24 wt %), Se (0.10–0.34 wt %), and Au (0.00–0.83 wt %) (ESM 1 Table S4). The atomic ratios of (Bi + Pb)/(S + Te) are between 0.76 and 0.86 (n = 14; mean = 0.80).

In Stage 3, this phase commonly appears as isolated grains with elongated shape and variable size in quartz, or at the margins of pyrrhotite. It can also be found with native gold, bismuthinite, ingodite, and joséite-B (Fig. 7g, j), and locally, intergrown with chalcopyrite. Compositionally, Stage 3 unnamed $(Bi,Pb)_3(Te,S)_4$ is similar to stage 2, with up to 0.29 wt % Sb, 0.30 wt % Se, 0.79 wt % Au, and (Bi + Pb)/(S + Te) atomic ratios of 0.74–0.82 (n = 8; mean = 0.78), but can be distinguished by its lower Pb (2.07–4.34 wt %) (ESM 1 Table S4).

A similar phase was reported from the Beiya skarn ores by Zhou et al. (2016). Chemically, $(Bi,Pb)_3(Te,S)_4$ from Stages 2 and 3 differ from that from Beiya by elevated (usually > 0.10 wt %) Au and Se contents (ESM 1 Table S4), making $(Bi,Pb)_3(Te,S)_4$ a significant gold-carrier (Ciobanu et al. 2009). In addition, the Stages 2 and 3 unnamed $(Bi,Pb)_3(Te,S)_4$ are Cu-deficient compared to the Beiya phase, that contains up to 0.65 wt % Cu (Zhou et al. 2016), reflecting the chemistry of the ore fluids associated with of porphyry Cu-(Mo)-Au and skarn Fe-Cu-Au mineralization at Beiya (Zhou et al. 2016).

Bi-Pb sulfosalts

The Bi-Pb sulfosalts are common in Stage 2 veins and consist of cosalite and galenobismutite. Cosalite appears as elongated lamellae or irregular blebs in pyrite, quartz, and chlorite, and as isolated grains or in assemblages with a variety of minerals, including electrum, joséite-B, unnamed $(Bi,Pb)_3(Te,S)_4$, and lillianite-gustavite solid solutions (Fig. 8a, b). Cosalite is Cu- (0.40–0.93 wt %), and Ag-rich (1.67–1.97 wt %) and contains variable amounts of Au (0–0.59 wt %), and Se (0.14–0.26 wt %) (ESM 1 Table S5). As a result of its high Cu and Ag contents, Wulong cosalite is compositionally close to the lillianite-gustavite join rather the ideal composition in the (Bi + Pb)-(Ag + Cu)-Pb ternary diagram (Fig. 6b), similarly to cosalite from the Beiya porphyry-skarn Cu-Fe-Au deposit (Zhou et al. 2016) and the Stanos shear-zone related Au deposit (Voudouris et al. 2013).

Galenobismutite is less abundant than cosalite and is found in the following associations in quartz: galenobismutite + unnamed $(Bi,Pb)_3(Te,S)_4$; galenobismutite + unnamed $(Bi,Pb)_3(Te,S)_4$ + electrum, and galenobismutite + unnamed $(Bi,Pb)_3(Te,S)_4$ + electrum + native bismuth (Fig. 8c). EPMA data indicate its composition close to the ideal stoichiometry (Fig. 6b and ESM 1 Table S5).

Bi-Pb-Ag and Bi-Ag sulfosalts

The Bi-Pb-Ag sulfosalts are another important group of Bi minerals in Stage 2 at the Wulong deposit. Based on their compositions, they comprise lillianite-gustavite solid solutions, vikingite, eskimoite, and galena-matildite series (Fig. 6b). In order to describe the different homologues, the ^{N}L terminology is used, where N represents the number of PbS-octahedra within the crystal structure (Makovicky 1977; Makovicky and Karup-Møller 1977a, b; Makovicky and Topa 2014). The calculation of N is based on the ideal formula $Pb_{N-1-2x}Bi_{2+x}Ag_xS_{N+2}$, where x is the Ag + Bi ↔ 2Pb substitution coefficient with $x_{max} = (N-2)/2$ (detail in Makovicky and Karup-Møller 1977a). Based on this, ^{4}L homologues in this study are related to lillianite-gustavite solid solutions, whereas vikingite and eskimoite belong to the ^{6}L and ^{7}L homologues, respectively (Fig. 6b and ESM 1 Table S6).

All analyzed phases of ^{4}L homologues (N values 3.47 to 3.95) are between the lillianite and gustavite end-members except one close to ideal gustavite (Fig. 6b). The intermediates commonly form elongated lamellae coexisting with cosalite, unnamed $(Bi,Pb)_3(Te,S)_4$, ingodite, joséite-B, and electrum in pyrite and quartz (Fig. 8b, d). They contain small ranges in Ag (3.04–5.95 wt %), elevated Au (0.09–0.59 wt %), Te (0.10–0.41 wt %), and Se (0.10–0.26 wt %), and are Cu- and Sb-deficient (ESM 1 Table S6). These intermediates can be further divided into two groups (Groups 1 and 2) according to L values (Fig. 6b). Group 1 has the highest gustavite component (L values 53.85 to 69.30%) and is characterized by 4.57–5.95 wt % Ag and 28.50–33.47 wt % Pb (ESM 1 Table S6). In contrast, Group 2 has a slightly higher lillianite component (L values 37.13 to 40.25%), and is characterized by higher Pb (37.70–38.56 wt %) but lower Ag (3.04–3.47 wt %) contents (ESM 1 Table S6). The phase close to ideal gustavite is rare and found in quartz, appearing as larger irregular grains or small blebs containing hessite inclusions. In general, they partly replaced joséite-B along its margin (Fig. 8e). One EPMA analysis gave 19.76 Pb wt %, 55.27 wt % Bi, 8.95 wt % Ag, and 16.48 wt % S, other trace elements being virtually absent (ESM 1 Table S6).

The ^{6}L homologue mineral is identified as vikingite (Fig. 8f). Only one elongated and irregularly shaped crystal of vikingite, embedded in quartz, was found in this study. An EPMA analysis gave 29.02 Pb wt %, 47.12 wt % Bi, 9.36 wt % Ag, and 15.97 wt % S, and minor Au (0.47 wt %), Te (0.25 wt %), and Se (0.22 wt %) (ESM 1 Table S6).

Eskimoite is a relatively abundant Bi-Pb-Ag sulfosalts at Wulong. It occurs in contact with electrum, joséite-B, hessite, and galena-matildite series (Fig. 8g). This phase has 10.11 to 12.09 wt % Ag and contains high Au (up to 0.65 wt %), Te (up to 0.84 wt %), and Se (up to 0.33 wt %) (ESM 1 Table S6). The N values are slightly higher than the ideal ^{7}L homologues (at 7.14–9.74) (ESM 1 Table S6). In the ternary (Bi + Sb)-(Ag + Cu)-Pb diagram, they plot near the ideal eskimoite position (Fig. 6b).

The galena-matildite series minerals in the Wulong deposit have, in most cases, completely or partly broken down to matildite and galena (Fig. 8g). Solid solution between matildite and galena is complete above 215 ± 15 °C (Craig 1967); hence the galena-matildite textures indicate crystallization above 215 ± 15 °C. This primary phase is located along the galena-matildite join, between the intermediate $Pb_7Ag_3Bi_3S_{13}$ and galena end members (Fig. 6b). The galena-matildite series occurs as large patches in quartz, and rarely at the margin of pyrite. They commonly contain small hessite inclusions, and can be enclosed or partly replaced by eskimoite (Fig. 8g). Intergrowths with electrum and chenguodaite ($Ag_9Fe^{3+}Te_2S_4$) are also observed. Chemically, the undecomposed phases have Ag ranging from 2.16 to 3.14 wt %, and high Au (0.50 to 0.80 wt %), Te (0.05 to 0.51 wt %), and Se (0.11 to 0.28 wt %) (ESM 1 Table S6). In the decomposed phases, matildite (Bi-Ag sulfosalts) occurs as thin (< 1 µm) lamellae up to ~ 100 µm in length in galena (Fig. 8g). The EDS analyses show that the lamellae have 52.70–55.10 wt % Bi, 29.30–30.70 wt % Ag, and 15.60–17.00 wt % S (ESM 1 Table S7).

Au-bearing bismuth phases

The Au-bearing Bi phases include maldonite (Au_2Bi), and jonassonite ($AuBi_5S_4$) (ESM 1 Table S7). Maldonite occurs in Stage 2 as small grains (< 5 µm) hosted within Au-Bi-Te or Au-Bi-Te-S droplets in the Bi mineral inclusion trails (Fig. 5c, d). In these droplets, mutual boundaries between maldonite and accompanying phases are curvilinear or nearly straight (Fig. 5c, d). Triple-point junctions are observed between maldonite, hedleyite, and native bismuth, indicating crystallization at equilibrium (Fig. 5d).

Jonassonite occurs in Stage 3 as stubbly grains occurring together with joséite-B and bismuthinite in large patches (Fig. 8h), as small irregular grains filling fractures in quartz, or as coexisting with native gold in small blebs (Fig. 8i). In the latter, cuspate boundaries between jonassonite and native gold are nearly straight (Fig. 8i).

Gold occurrences

In Stage 2, Au mainly occurs as electrum, with minor native gold. Visible gold is located in four textural settings: (setting I of stage 2, abbreviated S2I) isolated inclusions in pyrite, filling microfractures in pyrite, or at the margins of pyrite (Fig. 9a), (S2II) isolated inclusions in quartz (Fig. 9b), (S2III) composite grains with Bi minerals (Fig. 9c), and (S2IV) isolated grains in the vicinity of Bi minerals (Fig. 9d). Texture types S2III and S2IV are most common (Fig. 9e), and located in pyrite, quartz or chlorite matrix. Type S2III gold is closely associated with a wide variety of Bi minerals, including native bismuth (Fig. 4a), bismuthinite (Figs. 4a, 5e, 9c), Bi-Pb sulfosalts (cosalite and galenobismutite) (Fig. 8a, c), Bi-Pb-Ag sulfosalts (lillianite-gustavite series, eskimoite, and galen-matildite series) (Fig. 8d), and Bi-sulfotellurides (joséite-A, joséite-B and unnamed $(Bi,Pb)_3(Te,S)_4$) (Figs. 7c, e, 9c). This type of gold is highly variable in size (< 2 to 150 µm), and is present as inclusions dispersed throughout these Bi minerals, or toward their edges (Figs. 4a, 7c, 8a, c, d). Gold grain shapes are dominantly well-rounded to sub-rounded, with minor angular to irregular shapes associated with filling the fractures in pyrite and quartz. Importantly, boundaries between gold and Bi minerals are commonly curvilinear or straight (Figs. 4a, 8a, c, d). In general, in settings S2I, S2II, and S2III electrum (20.45 to 45.90 wt % Ag; n = 27; mean = 30.63 wt %; ESM 1 Table S7) occurs in large composite patches (Figs. 4a, 7c, 8a, c, d), whereas native gold is located in small Bi mineral inclusion trails (Fig. 5e and ESM 1 Fig. S5c).

In Stage 3, Au mineralization is characterized by native gold (Ag content 5.81 to 12.90 wt %; ESM 1 Table S8) in five textural settings, including (in order of abundance): (setting I of stage 3, abbreviated S3I) as isolated grains in pyrite (Fig. 9f), (S3II) as isolated grains in pyrrhotite (Fig. 9g), (S3III) as isolated grains in quartz (Fig. 9h), (S3IV) as isolated grains situated in the vicinity of Bi minerals (Fig. 9i), and (S3V) as grains in composite patches and blebs with a variety of Bi minerals (Fig. 9j, k), including native bismuth, bismuthinite, unnamed Bi_8Te_3, joséite-A, joséite-B, unnamed $(Bi,Pb)_3(Te,S)_4$, ingodite, and jonassonite (Figs. 4e, f, 5h, 7g-j and 8h, i). Textural types S3I, S3II, and S3III are observed as rounded to sub-rounded grains, rarely exceeding 50 µm in size, whereas types S3IV and S3V are present as elongated to rounded droplets or more rarely as lamellae up to 90 µm in length. Spatially, the type S3V gold is completely or partly enclosed by Bi minerals, and situated along their boundaries, with up to 7 native gold grains > 5 µm across in a single patch (Fig. 7j). The boundaries between gold and Bi minerals are again sharp and curvilinear.

The close Bi-Au association

Petrographic observations indicate that visible gold is positively correlated with the Bi minerals at the Wulong gold deposit. From a total of 1348 gold grains identified in Stage 2, textural type S2I gold accounts for ~ 11%, type S2II for ~ 4%; type S2III for ~ 61%; and type S2IV for ~ 24%. That is, almost 85% of the observed gold grains are spatially associated with Bi minerals in Stage 2 (Fig. 9e). In Stage 3, the gold textural types S3IV and S3V, which are spatially related to Bi minerals, are responsible for approximately 19% and 66% of the visible gold, respectively ($n = 1359$; Fig. 9l). This intimate Bi-Au association is supported by the whole-rock geochemical data of gold ores from Stages 2 and 3 (ESM 1 Table S8), which reveals a strong positive correlation between Bi and Au, and Bi/Au ratios consistently > 10 (Fig. 10).

Discussion

Chemical evolution in the hydrothermal fluids at reduced conditions

The chemical conditions of ore deposition at Stages 2 and 3 are shown in Fig. 11a as a function of $fTe_2(g)$ versus $fS_2(g)$.

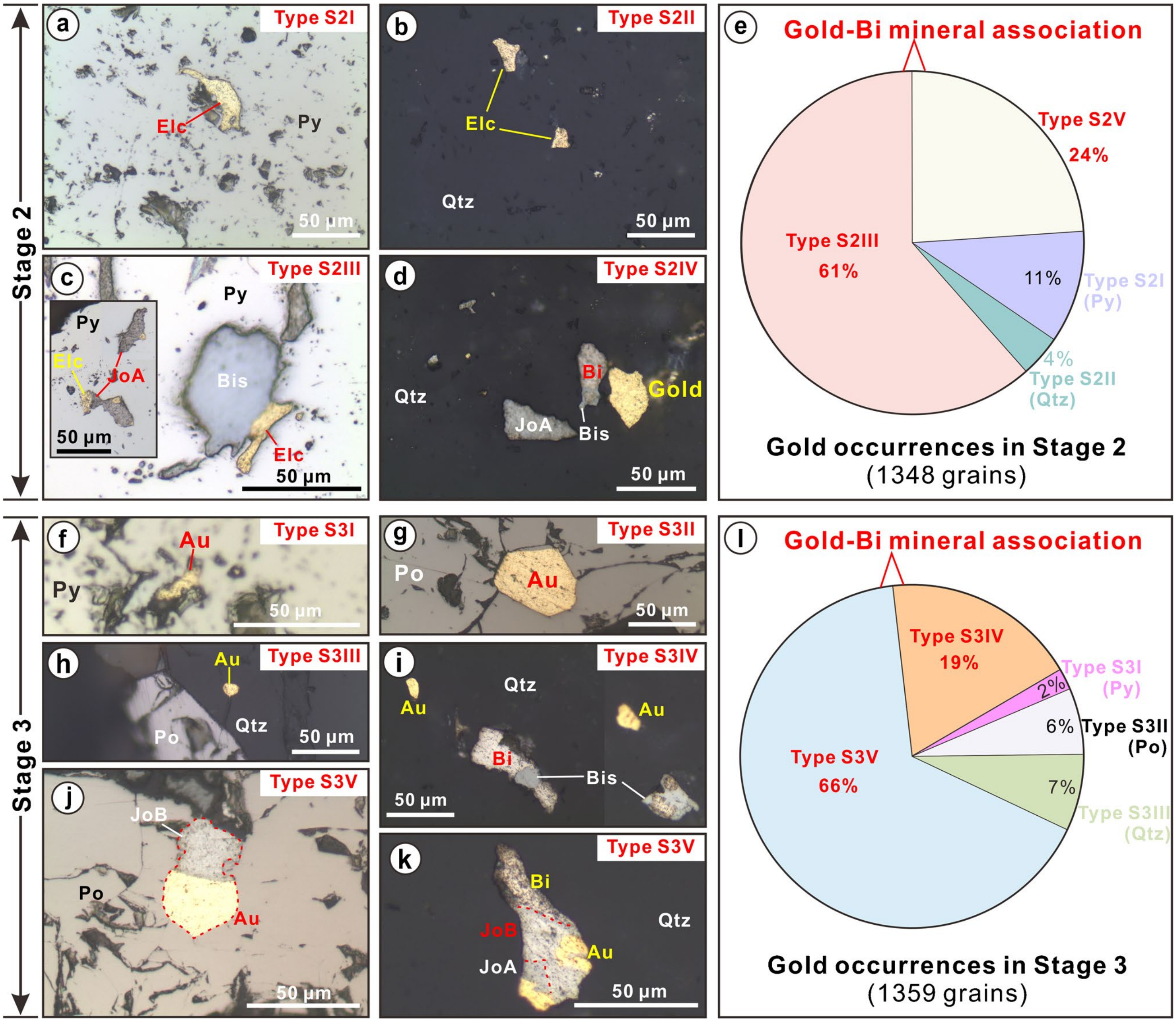

Fig. 9 Reflected-light photomicrographs (**a-d** and **f-k**) and pie chart (**e** and **i**) showing visible gold occurrences in Stages 2 and 3 auriferous quartz veins at the Wulong gold deposit. **a** Type S2I gold inclusion (electrum) in pyrite. **b** Type S2II gold (electrum) hosted in quartz. **c** Type S2III gold (electrum) coexisting with bismuthinite and joséite-A in two-component blebs hosted by pyrite. **d** Type S2IV gold nearby the blebs of native bismuth and joséite-A in quartz. **e** Pie chart illustrating the percentage of various types of gold in Stage 2. **f** Type S3I gold (native gold) hosted in pyrite. **g** Type S3II gold (native gold) hosted in pyrrhotite. **h** Type S3III gold (native gold) hosted in quartz, in which Bi minerals were not observed. **i** Type S3IV gold (native gold) in quartz nearby the native bismuth blebs that were partly replaced by bismuthinite. **j** Type S3V gold (native gold) intergrown with joséite-B in a two-component, droplet-like bleb in pyrrhotite. **k** Type S3V gold (native gold), native bismuth, joséite-A, and joséite-B in a quartz-hosted bleb. **l** Pie chart illustrating the percentage of various types gold in Stage 2. Abbreviations: Au = native gold, Bis = bismuthinite, Elc = electrum, JoA = joséite-A, JoB = joséite-B, Po = pyrrhotite, Qtz = quartz

The conditions chosen are 300˚C and 100 bars; temperatures are consistent with chlorite thermometry (291° to 336 °C; ESM 1 Table S9) and previous fluid inclusion studies (Yu et al. 2018). The field of Stage 2 is constrained by the coexistence of pyrite ± pyrrhotite, native bismuth ± bismuthinite, and the presence of hessite but absence of metallic silver. The field of Stage 3 is constrained by the predominance of pyrrhotite ± pyrite, presence of galena but no altaite; native gold but no calaverite; and native bismuth, with bismuthinite always a late replacement of native bismuth (ESM 1 Fig. S3). The main difference is slight lowering of the S_2(g) fugacity from Stage 3 to Stage 2.

The fugacities of S_2(g) and Te_2(g) are related to the amounts of sulfur in solution and to redox (e.g., fO_2(g);

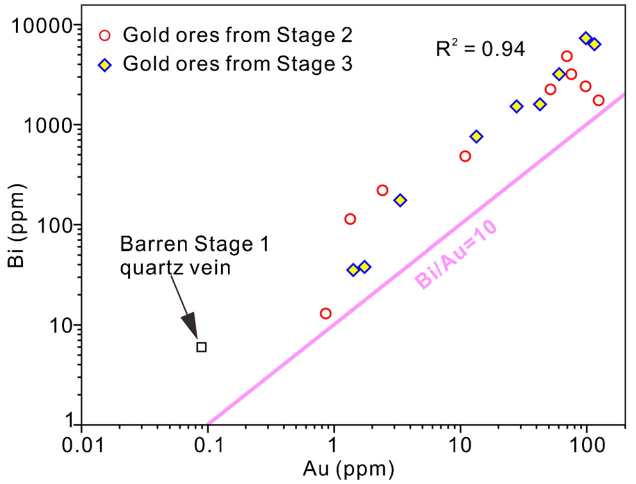

Fig. 10 Scatter plot of Bi versus Au for auriferous quartz ores of Stages 2 and 3. Note that the pink line represents the Bi/Au ratio of 10:1

Fig. 11b). Although the thermodynamic properties of most sulfosalts remain poorly constrained (Craig and Barton 1973), the tetradymite group has previously been used to constrain the redox conditions based on the Bi/(Te + S + Se) ratio compared with empirical mineral assemblages (Cook and Ciobanu 2004; Ciobanu et al. 2005, 2010). Phases with Bi/(Te + S + Se) ratios > 1 are associated with relatively more reduced conditions, and co-exist with native bismuth, maldonite, and jonassonite, whereas phases with Bi/(Te + S + Se) ratios < 1 are related to more oxidized environments, and co-exist with native tellurium and gold tellurides (Ciobanu et al. 2005, 2010). At the Wulong gold deposit, Bi-sulfotellurides (joséite-A, and joséite-B) with Bi/(Te + S + Se) ratios > 1 are common in Stage 2, as well as rare (only one sample) tetradymite with Bi/(Te + S + Se) ratios < 1. Given the ubiquitous presence of CO_2-CH_4-rich fluid inclusions in quartz (Yu et al. 2018), and that minor pyrrhotite is observed, we suggest that such assemblages indicate a reduced environment (close to pyrite-pyrrhotite buffer), but with local fluctuations of oxygen fugacity. In Stage 3, all tellurides and Bi-sulfotellurides (hedleyite, unnamed Bi_8Te_3, joséite-A, and joséite-B) have Bi/(Te + S + Se) ratios > 1, suggesting more reduced conditions in the pyrrhotite stability field. These conditions are consistent with the occurrences of native bismuth, jonassonite (Figs. 4d, e, and 8h, i), and abundant pyrrhotite (Fig. 3g and ESM 1 Fig. S2c). Since redox conditions in Stages 2 and 3 were buffered to reduced conditions due to the coexistence of CO_2 and CH_4 in the fluid (Fig. 11b), the differences in paragenesis between Stages 2 and 3 (ESM 1 Fig. S3) are unlikely to be due to small changes in redox. Changes in $f S_2$(g) (lower in Stage 3; Fig. 11a), and Bi availability (higher in Stage 3) are the most important factors affecting the evolution from Stage 2 to Stage 3.

There are obvious distinctions in the mineral associates between Stages 2 and 3. The former is characterized by widespread Ag-rich Bi-sulfosalts and tellurides (hessite), whereas the later contains abundant Ag-deficient Bi-Te minerals. In Stage 2, textural relationships suggest that the Bi minerals crystallized in order as follows: native

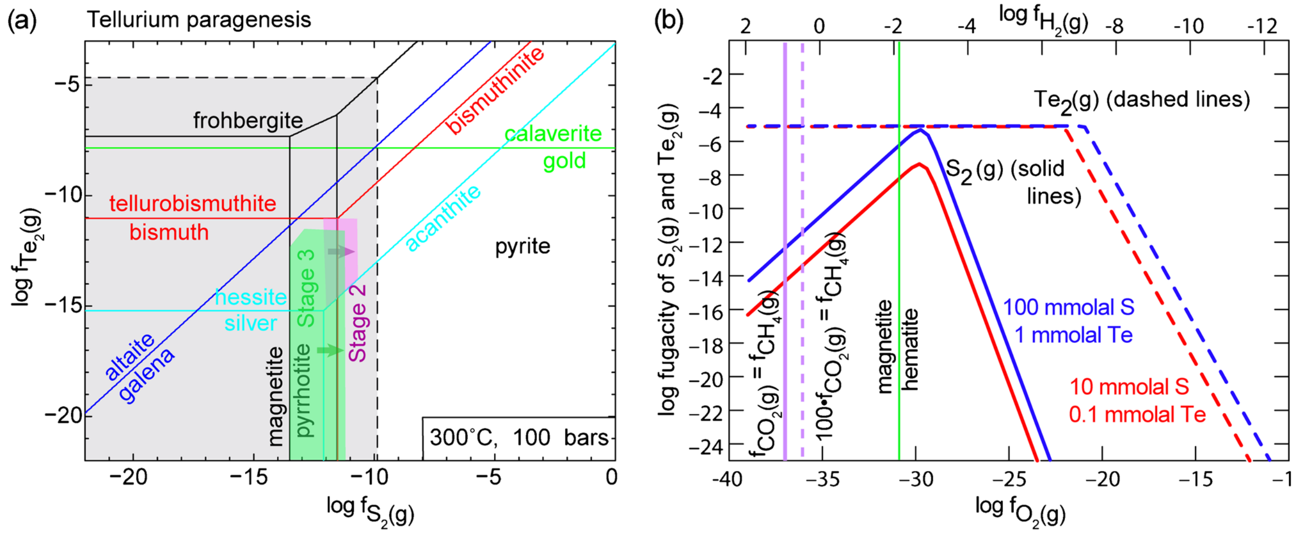

Fig. 11 Log f_{Te2}—Log f_{S2} diagram at 300 °C and 100 bars illustrating conditions of mineral deposition during Stages 2 and 3 at the Wulong gold deposit. In (**a**), the magnetite boundaries were plotted at fH_2(g) of 1 (solid line) and 0.01 (dashed line); pyrrhotite is stable at $fH_2(g) > 0.19$. The thermodynamic data are similar to those used by Mueller et al. (2020); native bismuth and bismuthinite are taken from Tooth et al. (2008), and those of tellurobismuthite from Robie and Hemingway (1995), retrieved from HSC Chemistry 9 (Outotec). The diagram **a** was drawn using the CHNOSZ package (Dick 2008), and **b** using Geochemist Workbench (Bethke 2008)

bismuth + hedleyite + maldonite → bismuthinite + Bi-sulfotellurides → Bi-Pb-Ag sulfosalts + hessite → Bi-Pb sulfosalts → unnamed $(Bi,Pb)_3(Te,S)_4$, although precipitation of distinct Bi minerals may partly overlap (ESM 1 Fig. S3). Chemically, Bi minerals in this sequence are characterized by an initial increase followed by a decrease in Ag and Pb concentrations (Fig. 12). Interestingly, gold in Stage 2 is present as native gold in early, small Bi mineral inclusion trails (Fig. 5e), and subsequently appears as electrum in later Bi mineral patches or blebs (Figs. 4a, 7c, 8a, c, d). In Stage 3, the early Bi minerals are Pb-Ag-poor (native bismuth and Bi-tellurides), followed by Pb-bearing Bi-sulfotellurides (joséite-A, joséite-B, ingodite, and $(Bi,Pb)_3(Te,S)_4$) (Fig. 12 and ESM 1 Fig. S3).

Previous studies have proposed that crystallization of diverse Bi-sulfosalts could result from fluctuating chemical gradients of Cu, Pb, Ag, and Bi in an ore system (Cook and Ciobanu 2003; Meisser et al. 2007; Zhou et al. 2016, 2018). For example, at the Yaoan gold deposit (South China block), an increase in the Ag contents from early bismuthinite derivatives to late padĕraite and cuprobismutite homologues was interpreted as indicating that the fluid was initially Ag-deficient and then became Ag-rich (Zhou et al. 2018). Replacement textures of Bi minerals, similar to those described at Yaoan, are recorded at Wulong (e.g., Figs. 4a, e, 7 and 8). Therefore, we propose that the composition and paragenetic evolution of Bi minerals from Stages 2 to 3 at Wulong likely resulted from fluctuations in the chemistry of the hydrothermal fluids. During Stage 2, these fluids were initially poor in Pb and Ag, and subsequently evolved to Pb- and Ag-rich solutions, but Pb and Ag concentrations decreased again (Fig. 12). Stage 3 fluids were initially Pb- and Ag-poor, but Pb concentrations subsequently increased slightly (Fig. 12); this is consistent

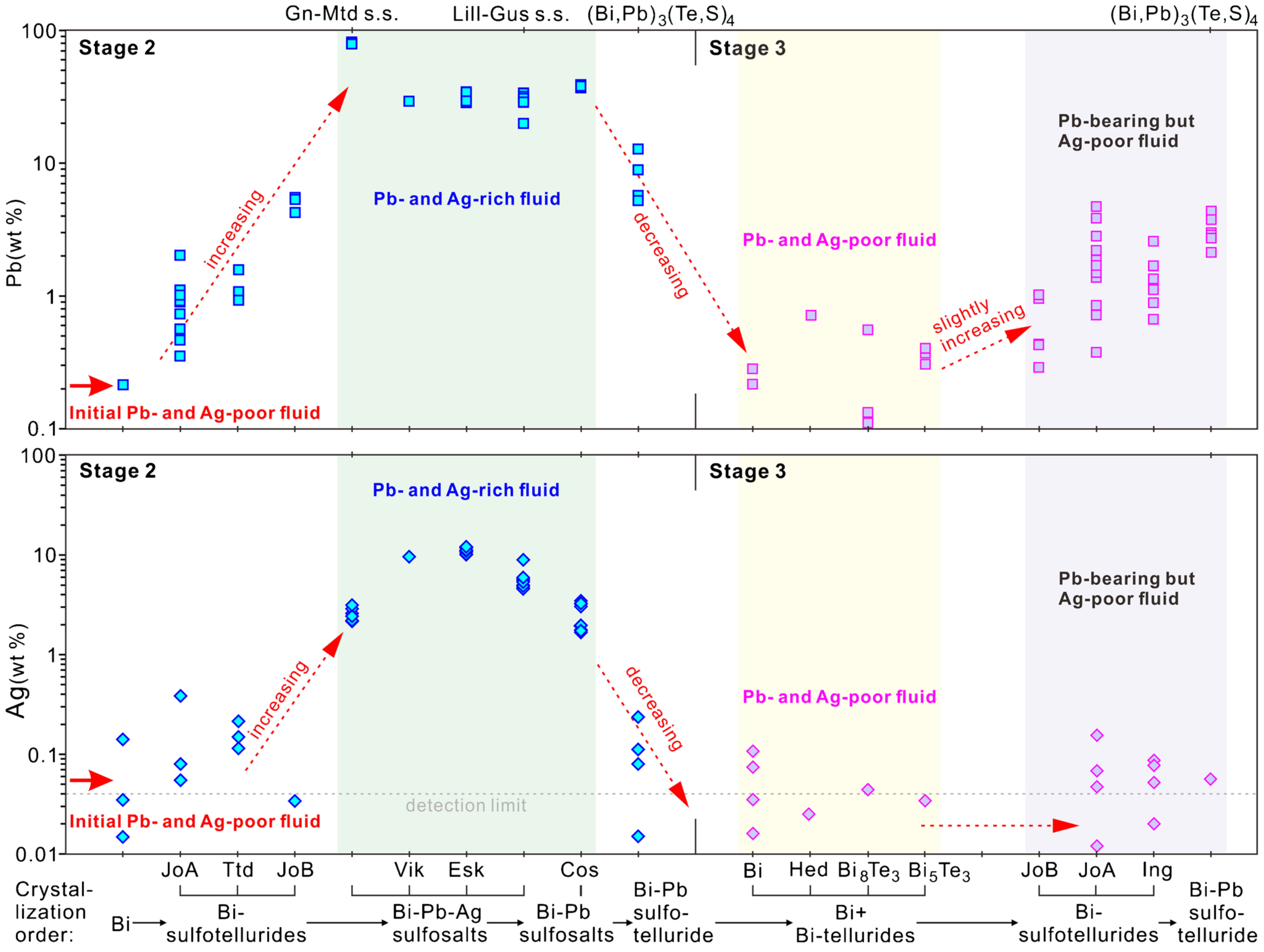

Fig. 12 Variations in Ag and Pb contents in typical Bi minerals relative to their crystallization order at the Wulong gold deposit, revealing the chemical evolution of ore-forming fluids from Stages 2 to 3. Abbreviations: Bi = native bismuth, Esk = eskimoite, Cos = cosalite, Gn-Mtd s. = galena-matildite solid solutions, Hed = hedleyite, Ing = ingodite, JoA = joséite-A, JoB = joséite-B, Lil s.s. = Lillianite-gustavite solid solutions, Ttd = tetradymite, Vik = vikingite

with the later occurrences of galena (Fig. 3g and ESM 1 Fig. S4c).

Liquid bismuth collector responsible for gold enrichment

Yu et al. (2018) reported that Au forms native gold grains in pyrite and quartz at the Wulong gold deposit. Based on fluid inclusion analysis, they suggested that Au deposition was directly triggered by fluid immiscibility that resulted in the destabilization of $Au(HS)_2^-$ complexes because of the exsolution of $H_2S(g)$ (Yu et al. 2018). In contrast, Wei et al. (2021) proposed a different Au deposition model of Bi-(Te)-rich melts as gold scavenger. Our study provides further evidence for the prevalence of the Bi-(Te)-rich melt gold scavenger mechanism: whole-rock concentrations of Au and Bi (Fig. 10); the widespread presence and close textural and temporal association of gold and Bi minerals in gold-rich samples (Fig. 9e, l); as well as the high Au contents of Bi minerals (up to 1.43 wt%; ESM 1 Table S3) are all expected features of this Au scavenging mechanism. However, contrary to Wei et al. (2021) who argue for a single depositional stage, we suggest that gold precipitation occurred over two main stages, as a result of elevated concentrations of Bi in Stages 2 and 3 fluids.

Stages 2 and 3 were both characterized by reduced hydrothermal fluids, supported by the CH_4-rich nature of the fluid inclusions, and the widespread occurrence of tetradymite group phases with Bi/(Te + Se + S) ratios > 1. Chlorite geothermometry indicates that the temperature of Stage 2 fluids was ~ 291° to 336 °C (ESM 1 Table S9). Yu et al. (2018) showed that quartz-hosted fluid inclusions from quartz-pyrite veins (Stage 2) have homogenization temperatures, interpreted as minimum trapping temperatures, exceeding 283 °C, and the quartz-polymetallic sulfide veins (Stage 3), have homogenization temperatures mostly between 250° and 328 °C, with outliers down to 219 °C. Hence, we suggest that the fluid temperatures during Stages 2 and 3 were favorable for precipitation of Bi-rich liquid under reduced conditions, given that native bismuth (melting point of 271 °C; Okamoto and Massalski 1983), Bi-Au eutectic (at 241 °C; Okamoto and Massalski 1983), Bi-Te eutectic (at 266 °C), and Bi-Te-Au eutectic (at 235 °C) would all be molten (Okamoto and Tanner 1990; Prince et al. 1990). The formation temperatures of the latter two melts are defined by the eutectics between native bismuth + hedleyite, and native bismuth + hedleyite + maldonite, respectively (Okamoto and Tanner 1990; Prince et al. 1990).

Petrographic observations strongly suggest that Bi-rich melts exsolved from Stages 2 and 3 fluids at Wulong. In both stages, large droplet-like blebs of native bismuth (Fig. 4d and ESM 1 Fig. S4a), and trails of small spherical Bi mineral inclusions are observed in quartz, near pyrite, pyrrhotite, or large Bi mineral patches (Fig. 5 and ESM 1 Fig. S5). Additionally, Stage 2 pyrite, and Stage 3 pyrrhotite and pyrite host multiphase Bi mineral droplets or blebs, consisting predominantly of native bismuth, bismuthinite, joséite-A, joséite-B, and gold (Fig. 9c, j and ESM 1 Fig. S4d), consistent with encapsulation of polymetallic melt droplets (e.g., Tomkins and Mavrogenes 2002; Tomkins et al. 2004; Sparks and Mavrogenes 2005; Törmänen and Koski 2005; Tomkins et al. 2007; Zhou et al. 2017). In the trails, hedleyite is common in the small droplets in Stages 2 and 3 (Fig. 5b-d, g, h). In addition, the Stage 3 trails contain the unnamed Bi_8Te_3 in the droplets (Fig. 5g, h). We thus suggest that both Bi-melt and Bi-Te-melt initially precipitated from Stage 2 and 3 fluids.

Immiscible Bi- and Bi-Te-melts can efficiently scavenge Au from hydrothermal fluids, forming Bi-Au melts and Bi-Te-Au melts, respectively (Douglas et al. 2000; Ciobanu et al. 2005; Wagner 2007; Tooth et al. 2008, 2011). This gold-scavenging process has been invoked to explain the intimate Bi-Au associations in many types of hydrothermal gold deposits, such as skarns (Ciobanu et al. 2003; Cockerton and Tomkins 2012; Kim et al. 2012; Zhou et al. 2017), orogenic gold (Ciobanu et al. 2006; Oberthür and Weiser 2008), porphyry-epithermal systems (Cook and Ciobanu 2004), IOCG-like systems (Acosta-Góngora et al. 2015), and volcanic-hosted massive sulfide deposits (Törmänen and Koski 2005). At the Wulong deposit, the same process is well preserved in the Stage 2 and 3 gold mineralization, as shown by the presence of numerous gold grains in the composite Bi mineral droplets and blebs (Figs. 4f, 5e, h and 9c, j, k), and the occurrence of maldonite (Au_2Bi) (Fig. 5c, d), and jonassonite ($AuBi_5S_4$) (Fig. 8h, i). The presence of Bi-Au melt is unavoidable when gold and native bismuth occur together in a system that formed at temperatures > 241 °C and under S-poor conditions (Fig. 11), and thus imply that all assemblages with these phases formed from melt. In Stage 2, three-component droplets of native bismuth, maldonite, and hedleyite (Fig. 5d), represent a typical texture resulting from cooling of Bi-Te-Au melt at 235 °C (Prince et al. 1990). In addition, we suggest that the droplets of maldonite and hedleyite in Stage 2 (Fig. 5c), the patches or blebs of jonassonite with gold (Fig. 8h, i), and the droplets of gold, native bismuth, hedleyite, and the unnamed Bi_8Te_3 in Stage 3 (Fig. 5h), crystallized from the

Bi-Te-Au melts. Within individual droplets and blebs, curvilinear and cuspate low-angle mutual boundaries abound (Figs. 5c-e, h and 8i), which are consistent with formation of the different components through Bi-melt crystallization (Ciobanu et al. 2006, 2010). Note that there are many bismuthinite droplets hosted in pyrite and quartz in Stages 2 and 3, and some contain gold grains (Figs. 4c, f, 9c and ESM 1 Fig. S4d). Since bismuthinite has a melting temperature of 775 °C, we propose that these droplets indicate sulfidation of preexisting Bi and Bi-Au melts, which was driven either by an increase in sulfur fugacity or by cooling (Tooth et al. 2011, 2013; Cockerton and Tomkins 2012; Zhou et al. 2017). Fluid cooling takes place inevitably over time (Yu et al. 2018), and an increase in sulfur fugacity is well recorded in Stage 2, where minor pyrrhotite has been enclosed by the widespread pyrite crystals (Fig. 3e). Textures consistent with late sulfidation of native bismuth are common in Stages 2 and 3 in the Wulong deposit, as shown by widespread replacement of native bismuth by bismuthinite (Fig. 4a, d, e). As a result, the native bismuth melts transform into bismuthinite droplets (Fig. 4c), whereas the Bi-Au melts transform into a stable assemblages of gold and bismuthinite (Figs. 4f, 9c). Such an interpretation has been invoked previously to explain the locally poor preservation of native bismuth in apparently molten, gold-bearing multiphase assemblages in many deposits (Tooth et al. 2011; Cockerton and Tomkins 2012; Zhou et al. 2017).

Thermodynamic modeling has shown that a deposit containing only 100 ppm Bi deposited as Bi melt from fluids containing only 0.2 ppb Au (i.e., strongly undersaturated relative to native gold) would attain Au grades of 5 ppm (Tooth et al. 2008). At Wulong, our geochemical analyses indicate Bi concentrations of up to 7332 ppm, with most ores containing > 100 ppm Bi (ESM 1 Table S8). The Bi/Au ratios are consistently above 10 (Fig. 10). The average gold grade of this deposit is 5.35 g/t (Wang et al. 2018); therefore, if all Bi initially precipitated as a liquid, it would be more than sufficient to scavenge all of the Au in the deposit from unsaturated fluids. The close Bi-Au association implies that this is a distinct possibility.

Why is the Wulong deposit unique in the NCC?

Trace amounts of Bi- and/or Te-bearing minerals are recorded in many Early Cretaceous hydrothermal gold deposits in the NCC (Gu et al. 2003; Bi et al. 2011; Zhou et al. 2011; Li et al. 2006, 2012a, b; Xu et al. 2014; Yang et al. 2016b). However, until now, the liquid bismuth collector model has not been invoked to explain the Au enrichment in the NCC, except for Wulong (Wei et al. 2021). The hydrothermal fluids at Wulong were characterized by high concentrations of Bi, resulting in higher Bi concentrations in the ores than those of Te and Bi/Te ratios > 1 in most Bi-Te phases; tellurides are rare (hessite). In contrast, the other Bi- and Te-bearing gold deposits in the NCC are dominated by native tellurium, Au- and/or Ag-tellurides; Bi-Te-bearing phases are minor and have Bi/Te ratios < 1 (e.g., tellurobismuthite, rucklidgeite, and volynskite) (Li et al. 2006, 2012a, b; Bi et al. 2011; Jian et al. 2014; Xu et al. 2014; Yang et al. 2016b). These mineralogical features indicate a strong enrichment in Te relative to Bi (Te > > Bi). This difference has significant implications for whether a Bi-bearing melt can form. In the Bi-rich part of the Bi-Te-Au ternary, the eutectic is located at 235 °C (Prince et al. 1990), whereas a thermal divide appears at Bi = Te, such that when Te > Bi, the ternary eutectic is slightly below 416 °C (Fig. 2). Almost all hydrothermal Au deposits in the NCC formed below this temperature (Jiang et al. 1999; Jiang 2000; Fan et al. 2003; Li et al. 2012b; Yang et al. 2015, 2016a, 2017; Guo et al. 2017), although the temperatures of barren, early stage fluids can be up to 417 ℃ in rare cases (Zhou et al. 2014; Fan et al. 2016).

Possible source of bismuth and tellurium

The abundance of Bi-Te minerals in quartz veins indicates that the ore-forming fluids in the Wulong gold deposit were enriched in bismuth and tellurium. As mentioned above, there can be significant amounts of Bi in both intrusion-related magmatic-hydrothermal and orogenic gold deposits. However, previous workers have suggested that Te in most gold deposits tends to be derived from magma (Afifi et al. 1988; Jensen and Barton 2000; Cooke and McPhail 2001). Tellurides are mostly identified in ore systems genetically related to magmatism (e.g., porphyry Cu deposits, epithermal Au deposits, IOCG, and intrusion-related Au deposits), and some orogenic gold deposits with magmatic affinity, for example the Golden Mile near Kalgoorlie (Hart 2007; Goldfarb et al. 2017; Spence-Jones et al. 2018; Missen et al. 2020; McDivitt et al. 2021). Some Te-enriched silicate melts may be derived from the partial melting of metasomatized mantle that was Te enriched by fluids/melts derived from ocean-floor sediments (Jensen and Barton 2000; Cook et al. 2009; Saunders and Brueseke 2012; Holwell et al. 2019). Such Te-enriched magmas and related ore deposits are commonly found around the Pacific Rim in subduction settings (e.g., epithermal Au-Te systems; Cook et al. 2009; Saunders and Brueseke 2012), and the Tethyan belt in post-subduction settings (e.g., Te-Pt–Pd-enriched porphyry Cu-Au deposits; Holwell et al. 2019). Alternatively, Tomkins et al. (2009) proposed that partial melting of preexisting zones of Au enrichment in the lower crust could also generate reduced, Au- and, Te-rich felsic magmas, which could also be enriched in Ag, As, Bi, and Sb.

Based on geological, geochemical and geochronological data, we propose that the Wulong gold deposit has a magma-derived Bi and Te source. The Wulong gold deposit is similar in most respects to reduced intrusion-related gold systems (RIRGS; Lang et al. 2000; Lang and Baker 2001; Hart et al. 2002; Hart 2007). It has abundant sheeted arrays of thin auriferous quartz veins (Fig. 3c), ore mineral assemblages are characterized by pyrite-pyrrhotite-arsenopyrite, with accessory scheelite in quartz veins (Fig. 3e, g, h), and in particular, the Au-Bi-Te enrichment is characteristic of many RIRGS. Other similarities between Wulong and RIRGS include:

(1) Ore-forming fluids in the Wulong gold deposit are characterized by low to medium temperature (219–395 °C), CO_2-rich, low- to medium-salinity (0.18–8.95 wt % NaCl equiv.) aqueous fluids with traces of CH_4 and N_2 (Yu et al. 2018).

(2) H–O and S isotope studies indicate that the ore-forming fluids at the Wulong gold deposit were derived from a magmatic source (Yu et al. 2018; Zhang et al. 2020). Moreover, He-Ar and Pb isotope compositions of Au-bearing pyrite suggest that mantle components were involved in the gold mineralization (Yu et al. 2018; Liu et al. 2019; Zhang et al. 2020).

(3) Geologic mapping, field relationships, and petrographic observations indicate that the Wulong gold deposit is spatially associated with Early Cretaceous intrusive rocks, especially diorite dykes (Fig. 1b, c).

(4) SIMS U–Pb dating of hydrothermal rutile co-precipitated with gold (Feng et al. 2020), and $^{40}Ar/^{36}Ar$ dating of sericite in auriferous quartz veins (Liu et al. 2019), reveal that Au mineralization at Wulong deposit took place at ~ 122 Ma, which coincides with the emplacement of fine-grained diorite dykes that have sharp contact with the auriferous quartz veins in the same structures (dated at 120 ± 1 Ma and 119 ± 6 Ma; Zhang 2002; Zhang et al. 2020).

For the RIRGS in Scheelite Dome, Yukon, Canada, the related magmatic suite was suggested to be hybrid magmas that formed through mixing of crust-derived melts and ultrapotassic alkaline mantle melts (lamprophyres), generated by low percentage partial melting of metasomatized lithosphere that had been fertilized during prior subduction in an extensional setting (Mair et al. 2011; Groves et al. 2020). This mixing process allows some components of the ore system to be derived from the crust and others from the mantle (e.g., see Table 2 in Tomkins et al. 2012). The dykes in the Wulong deposit are consistent with this; there are many lamprophyre dykes (Fig. 1b, c), and dioritic melt compositions that tend to form by hybridization in MASH (mixing, assimilation, storage and hybridization) settings (Hildreth and Moorbath 1988; Annen et al. 2006). Regionally, the Au mineralization and magmatism at Wulong are in accord with a peak in the timing of destruction of the NCC (at ~ 125 Ma; Zhu et al. 2015, 2017), which was caused by subduction of the paleo-Pacific plate (Zhu et al. 2017; Wu et al. 2019). From the Early Jurassic, the lithospheric mantle beneath this region experienced metasomatism by melts/fluids derived from subducting paleo-Pacific slab (Zhu et al. 2017; Zheng et al. 2018; Wu et al. 2019). During this process, tellurium may have been enriched in metasomatized mantle domains. Subsequent destruction of the NCC in the Early Cretaceous, promoted by removal of mantle lithosphere and upwelling of hot asthenosphere, caused preferential melting of the metasomatized mantle domains, generating Te- and probably Au-rich magmas, whereas melting of a lower crustal component may have contributed W, Bi, and Pb (Gao et al. 2004; Tomkins et al. 2012). Variation in this lower crustal component would explain variations in ratios of the various metals in the Jiaodong Peninsula and the North China Craton in general.

Conclusions

The large Wulong gold deposit formed over four paragenetic vein stages, with abundant Bi minerals being co-deposited with economic Au during Stages 2 and 3. Mineralogically, Stage 2 is distinguished from Stage 3 by the associated Bi-Pb (cosalite and galenobismutite), and Bi-Pb-Ag sulfosalts (galena-matildite series, vikingite, eskimoite, and lillianite-gustavite series), and Ag-tellurides (hessite), and the absence of the unnamed Bi-tellurides (Bi_8Te_3 and Bi_5Te_3). Gold minerals in Stage 2 include maldonite, native gold and electrum, whereas jonassonite and native gold occur in Stage 3.

Importantly, Bi minerals in the two main mineralization stages (Stages 2 and 3) are significant hosts for gold. Given the presence of droplet-like blebs of native bismuth, and small, spherical Bi mineral inclusion trails and the temperature at the time of mineralization, we conclude that Bi precipitated from the hydrothermal fluids as a liquid. The presence of polymineralic blebs and small droplets in trails containing gold, maldonite, and jonassonite, is evidence that this liquid bismuth scavenged Au from fluids during Stages 2 and 3, and operated as the primary mechanism for gold deposit formation. The Wulong deposit has a strong enrichment in Bi relative to Te (Bi > > Te), and this is the main reason that the liquid bismuth collector operated at Wulong and not in most of the other Early Cretaceous hydrothermal gold deposits in the NCC. Wulong is likely to be an example of a reduced intrusion-related gold system, with Te sourced from metasomatized mantle during decratonization of the NCC, and metals like W, Pb and possibly Bi sourced from the lower crust; Au could plausibly have been sourced from either, but given the ubiquity across the NCC it is more likely to have been sourced from the mantle. From Stages 2 to 3, the chemical and paragenetic evolution of Bi minerals indicate fluctuations in Pb and Ag concentrations of the reduced (methane-bearing) ore-forming fluids, which may reflect variations in the relative proportions of mantle and crust contributions to the evolving source magmas.

Supplementary Information The online version contains supplementary material available at https://doi.org/10.1007/s00126-022-01120-4.

Acknowledgements We are grateful to Xin Yan for assistance with the SEM analysis, as well as Lihui Jia for help and guidance during the EMPA analysis. We also very much thank the Wulong Mining Ltd. for deposit access, and local geologist Jianping Li for providing assistance during fieldwork. We greatly appreciate the detailed and constructive comments and insightful suggestions of three anonymous reviewers, associate editor Steffen Hagemann and editor Georges Beaudoin, who helped us to significantly improve the quality of this manuscript.

Funding The research was jointly supported by the National Natural Science Foundation of China (91414301 and 91962213), and the International Partnership Program of International Cooperation Bureau, Chinese Academy of Sciences (132A11KYSB20190070).

Declarations

Competing interests The authors declare no competing interests.

References

Acosta-Góngora P, Gleeson SA, Samson IM, Ootes L, Corriveau L (2015) Gold refining by bismuth melts in the iron oxide-dominated NICO Au-Co-Bi (±Cu±W) deposit, NWT, Canada. Econ Geol 110:291–314

Afifi AM, Kelly WC, Essene EJ (1988) Phase relations among tellurides, sulfides, and oxides: II. Applications to telluride-bearing ore deposits. Econ Geol 83:395–404

Annen C, Blundy JD, Sparks RSJ (2006) The genesis of intermediate and silicic magmas in deep crustal hot zones. J Petrol 47:505–539

Bethke CM (2008) Geochemical and biogeochemical reaction modeling, 2nd edn. Cambridge Univ Press, New York

Bi SJ, Li JW, Zhou MF, Li ZK (2011) Gold distribution in Asdeficient pyrite and telluride mineralogy of the Yangzhaiyu gold deposit, Xiaoqinling district, southern North China craton. Mineral Deposita 46:925–941

Bi SJ, Li ZK, Tang KF, Gao K (2016) LA-ICP-MS in situ trace element analysis of pyrite from Dongtongyu gold deposit and its metallogenic significance, Xiaoqinling gold district. Earth Sci 41:1121–1140

Cepedal A, Fuertes-Fuente M, Martín-Izard A, González-Nistal S, Rodríguez-Pevida L (2006) Tellurides, selenides and Bi-mineral assemblages from the Río Narcea Gold Belt, Asturias, Spain: genetic implications in Cu–Au and Au skarns. Mineral Petrol 87:277–304

Ciobanu CL, Cook NJ, Bogdanov K, Kiss O, Vuèkoviæ B (2003) Gold enrichment in deposits of the Banatitic Magmatic and Metallogenetic belt. In: Eliopoulos DG et al (eds) Mineral Exploration and Sustainable Development. Millpress, Rotterdam, pp 1153–1156

Ciobanu CL, Cook NJ, Pring A (2005) Bismuth tellurides as gold scavengers. In: Mao JW, Bierlein FP (eds) Mineral deposit research: meeting the global challenge. Springer, Berlin, pp 1383–1386

Ciobanu CL, Cook NJ, Damian F, Damian G (2006) Gold scavenged by bismuth melts: An example from Alpine shear-remobilizates in the Highiş Massif, Romania. Mineral Petrol 87:351–384

Ciobanu CL, Birch WD, Cook NJ, Pring A, Grundler PV (2010) Petrogenetic significance of Au-Bi-Te-S associations: The example of Maldon, Central Victorian gold province, Australia. Lithos 116:1–17

Ciobanu CL, Cook NJ, Pring A, Brugger J, Danyushevsky LV, Shimizu M (2009) "Invisible gold" in bismuth chalcogenides: Geochimica et Cosmochimica Acta73:1970−1999

Cockerton ABD, Tomkins AG (2012) Insights into the liquid bismuth collector model through analysis of the Bi-Au Stormont skarn prospect, northwest Tasmania. Econ Geol 107:667–682

Cook NJ, Ciobanu CL (2003) Lamellar minerals of the cuprobismutite series and related paděraite: a new occurrence and implications. Can Mineral 41:441–456

Cook NJ, Ciobanu CL (2004) Bismuth tellurides and sulphosalts from the Larga hydrothermal system, Metaliferi Mts. Romania: Paragenesis and genetic significance. Mineral Mag 68:301–321

Cook NL, Ciobanu CL, Wagner T, Stanley CJ (2007) Minerals of the system Bi-Te-Se-S related to the tetradymite archetype: Review of classification and compositional variation. Can Mineral 45:665–708

Cook NJ, Ciobanu CL, Spry PG, Voudouris P (2009) Understanding gold-(silver)-telluride-(selenide) mineral deposits. Episodes 32:249–263

Cooke DR, McPhail DC (2001) Epithermal Au-Ag-Te mineralization, Acupan, Baguio district, Philippines: numerical simulations of mineral deposition. Econ Geol 96:109–131

Craig JR (1967) Phase relations and mineral assemblages in the Ag-Bi-Pb-S system. Mineral Deposita 1:278–306

Craig JR, Barton PB (1973) Thermochemical approximations for sulfosalts. Econ Geol 68:493–506

Dick JM (2008) Calculation of the relative metastabilities of proteins using the CHNOSZ software package. Geochem Trans 9:1–17

Douglas N, Mavrogenes J, Hack A, England R (2000) The liquid bismuth collector model: An alternative gold deposition mechanism. 15th Austral Geol Conv Abstr 59:135

Fan HR, Zhai MG, Xie YH, Yang JH (2003) Ore-forming fluids associated with granite-hosted gold mineralization at the Sanshandao deposit, Jiaodong gold province, China. Mineral Deposita 38:739–750

Fan HR, Zhai MG, Yang KF, Hu FF (2016) Late Mesozoic gold mineralization in the North China craton. In: Zhai MG, Zhao Y, Zhao TP (eds) Main tectonic events and metallogeny of the North China craton. Springer, Singapore, pp 511–525

Feng K, Fan HR, Hu FF, Yang KF, Liu X, Shangguan YN, Cai YC, Jiang P (2018) Involvement of anomalously As-Au-rich fluids in the mineralization of the Heilan'gou gold deposit, Jiaodong, China: Evidence from trace element mapping and, in-situ, sulfur isotope composition. J Asian Earth Sci 160:304–321

Feng HX, Shen P, Zhu RX, Li CH, Ma G, Pan HD (2019) Geology and He-Ar-S-Pb isotope constraints on the genesis of the Sidaogou gold deposit in Liaodong Peninsula, northeastern North China Craton. Ore Geol Rev 113:103080

Feng HX, Shen P, Zhu RX, Ma G, Li CH, Li JP (2020) SIMS U-Pb dating of vein-hosted hydrothermal rutile and carbon isotope of fluids in the Wulong lode gold deposit, NE China Linking Gold Mineralization with Craton Destruction. Ore Geol Rev 127:103838

Frost BR, Mavrogenes JA, Tomkins AG (2002) Partial melting of sulfide deposits during medium- and high-grade metamorphism. Can Mineral 40:1–18

Gao S, Rudnick RL, Yuan HL, Liu XM, Liu YS, Xu WL, Ling WL, Ayers J, Wang XC, Wang QH (2004) Recycling lower continental crust in the North China craton. Nature 432:892–897

Goldfarb RJ, Santosh M (2014) The dilemma of the Jiaodong gold deposits: Are they unique? Geosci Front 5:139–153

Goldfarb RJ, Berger BR, George MW, Seal RR (2017) Tellurium. US Geol Surv Prof Pap 1802:R1–R27

Groves DI, Zhang L, Santosh M (2020) Subduction, mantle metasomatism, and gold: A dynamic and genetic conjunction. Geol Soc Am Bull 132:1419–1426

Gu XP, Watanabe M, Hoshino K, Shibata Y (2003) New find of tellurosulphides from the Funan Gold Deposit, East Shandong, China. Eur J Miner 15:147–155

Gu YC, Chen RY, Li DT, Yang JL, Yang FC, Jia HX, Dick J, Hu QH, Ju N, Cao J, Li SZ (2018) Jurassic ca. 160 Ma crustal remelting and Paleoproterozoic intrusive rock residues in the Liaodong Peninsula, East China: Evidence from in situ zircon U-Pb dating and Lu-Hf isotopic analysis. Geol J 53:174–188

Guo LN, Goldfarb RJ, Wang ZL, Li RH, Chen BH, Li JL (2017) A comparison of Jiaojia- and Linglong-type gold deposit ore-forming fluids: Do they differ? Ore Geol Rev 88:511–533

Guo LN, Deng J, Yang LQ, Wang ZL, Wang SR, Wei YJ, Chen BH (2020) Gold deposition and resource potential of the Linglong gold deposit, Jiaodong Peninsula: Geochemical comparison of ore fluids. Ore Geol Rev 120:103434

Hart CJR, McCoy DT, Goldfarb RJ, Smith M, Roberts P, Hulstein R, Bakke AA, Bundtzen TK (2002) Geology, exploration and discovery in the Tintina gold province, Alaska and Yukon. Soc Econ Geol Spec Publ 9:241–274

Hart CJR (2007) Reduced intrusion-related gold systems. In Goodfellow WD (ed) Mineral deposits of Canada: A synthesis of major deposit types, district metallogeny, the evolution of geological provinces, and exploration methods. Geol Assoc Canada, Mineral Deposits Division, Spec Publ 5:95–112

Hey MH (1954) A new review of the chlorites. Mineral Mag 30:277–292

Hildreth W, Moorbath S (1988) Crustal contributions to arc magmatism in the Andes of central Chile. Contrib Mineral Petrol 98:455–489

Holwell DA, Fiorentini M, McDonald I, Lu YJ, Giuliani A, Smith DJ, Keith M, Locmelis M (2019) A metasomatized lithospheric mantle control on the metallogenic signature of post-subduction magmatism. Nat Commun 10:1–10

Jensen EP, Barton MD (2000) Gold deposits related to alkaline magmatism. Rev Econ Geol 13:279–314

Jian W, Lehmann B, Mao JW, Ye HS, Li ZY, Zhang JG, Zhang H, Feng JW, Ye YZ (2014) Telluride and Bi-sulfosalt mineralogy of the Yangzhaiyu gold deposit, Xiaoqinling region, central China. Can Mineral 52:883–898

Jian W, Mao JW, Lehmann B, Cook NJ, Xie GQ, Liu P, Duan C, Alles J, Niu ZJ (2021) Au-Ag-Te–rich melt inclusions in hydrothermal gold-quartz veins, Xiaoqinling lode gold district, Central China. Econ Geol 116:1239–1248

Jiang N (2000) Hydrothermal Fluid Evolution Associated with Gold Mineralization at the Wenyu Mine, Xiaoqinling District, China. Resour Geol 50:103–112

Jiang N, Xu J, Song M (1999) Fluid inclusion characteristics of mesothermal gold deposits in the Xiaoqinling district, Shaanxi and Henan Provinces, People's Republic of China. Mineral Deposita 34:150–162

Kim EJ, Park ME, White NC (2012) Skarn gold mineralization at the Geodo mine, South Korea. Econ Geol 107:537–551

Lang JR, Baker T (2001) Intrusion-related gold systems: The present level of understanding. Mineral Deposita 36:477–489

Lang JR, Baker T, Hart CJR, Mortensen JK (2000) An exploration model for intrusion-related gold deposits. Soc Econ Geol Newsletter 40:6–15

Li ZL, Xu WD, Qin QM, Pang WZ (1987) Geological characteristics and ore genesis of Wulong gold deposit, Liaoning Province. Contrib Geol Mineral Resour Res 2:31–39 (in Chinese with English abstract)

Li SZ, Zhao GC, Sun M, Han ZZ, Luo Y, Hao DF, Xia XP (2005) Deformational history of the Paleoproterozoic Liaohe Group in the Eastern Block of the North China Craton. J Asian Earth Sci 24:659–674

Li JW, Ma CQ, Vasconcelos P, Zhou MF, Zhao XF (2006) Geochronology of the Pengjiakuang and Rushan gold deposits, eastern Jiaodong gold province, Northeastern China: Implications for regional mineralization and geodynamic setting. Econ Geol 101:1023–1038

Li JW, Bi SJ, Sebly D, Chen L, Vasconcelos P, Thiede D, Zhou MF, Zhao XF, Li ZK, Qiu HN (2012) Giant Mesozoic gold provinces related to the destruction of the North China craton. Earth Planet Sci Lett 349–350:26–37

Li JW, Li ZK, Zhou MF, Chen L, Bi SJ, Deng XD, Qiu HN, Cohen B, Sebly D, Zhao XF (2012) The Early Cretaceous Yangzhaiyu lode gold deposit, North China craton: A link between craton reactivation and gold veining. Econ Geol 107:43–79

Li XH, Fan HR, Yang KF, Hollings P, Liu X, Hu FF, Cai YC (2018) Pyrite textures and compositions from the Zhuangzi Au deposit, southeastern North China craton: Implication for ore-forming processes. Contrib Mineral Petrol 173:73–92

Liu DY, Nutman AP, Compston W, Wu JS, Shen QH (1992) Remmants of ≥ 3800 Ma crust in the Chinese part of the SinoKorean Craton. Geol 20:339–342

Liu JL, Ji M, Shen L, Guan HM, Davis GA (2011) Early Cretaceous extensional structures in the Liaodong Peninsula: Structural associations, geochronological constraints and regional tectonic implications. Sci China Earth Sci 54:823–842

Liu JL, Shen L, Ji M, Guan HM, Zhang ZC, Zhao ZD (2013) The Liaonan/Wanfu metamorphic core complexes in the Liaodong Peninsula: Two stages of exhumation and constraints on the destruction of the North China Craton. Tectonics 32:1121–1141

Liu WH, Etschmann B, Testemale D, Hazemann JL, Rempel K, Müller H, Brugger J (2014) Gold transport in hydrothermal fluids: competition among the Cl-, Br-, HS- and NH_3(aq) ligands. Chem Geol 376:11–19

Liu J, Zhang LJ, Wang SL, Li TG, Yang Y, Liu FX, Li SH, Duan C (2019) Formation of the Wulong gold deposit, Liaodong gold Province, NE China: Constraints from zircon U-Pb age, sericite Ar-Ar age, and H-O-S-He isotopes. Ore Geol Rev 109:130–143

Lu XP, Wu FY, Lin JQ, Sun DY, Zhang YB, Guo CL (2004) Geochronological successions of the early Precambrian granitic magmatism in southern Liaodong peninsula and its constraints on tectonic evolution of the North China Craton. Chin J Geol 39:123–138 (in Chinese with English abstract)

Luo Y, Sun M, Zhao GC, Li SZ, Xu P, Ye K, Xia XP (2004) LA-ICP-MS U-Pb zircon ages of the Liaohe Group in the Eastern Block of the North China Craton: constraints on the evolution of the Jiao-Liao-Ji Belt. Precambrian Res 134:349–371

Mair JL, Farmer GL, Groves DI, Hart CJR, Goldfarb RJ (2011) Petrogenesis of postcollisional magmatism at Scheelite Dome, Yukon, Canada: Evidence for a lithospheric mantle source for magmas associated with intrusion-related gold systems. Econ Geol 106:451–480

Makovicky E (1977) Chemistry and crystallography of the lillianite homologous series. Part III. Crystal chemistry of lillianite homologues. Related Phases Neues Jahrb Mineral Abh 131:187–207

Makovicky E, Karup-Møller S (1977) Chemistry and crystallography of the lillianite homologous series. Neues Jahrb Mineral Abh 130:264–287

Makovicky E, Karup-Møller S (1977) Chemistry and crystallography of the lillianite homologous series. Part II: definition of new minerals: eskimoite, vikingite, ourayite and treasurite. Redefinition of schirmerite and new data on the lillianite-gustavite solidisolution series. Neues Jahrb Mineral Abh 131:187–207

Makovicky E, Topa D (2014) Lillianites and andorites: new life for the oldest homologous series of sulfosalts. Mineral Mag 78:387–414

McDivitt JA, Hagemann SG, Thébaud N, Martin LAJ, Rankenburg K (2021) Constraints on the structural setting, relative timing, and geochemistry of the Fimiston, Hidden Secret, and Oroya gold-telluride lode types, Kalgoorlie gold camp, Western Australia. Mineral Deposita. https://doi.org/10.1007/s00126-021-01077-w

Meisser N, Schenk K, Berlepsch P, Brugger J, Bonin M, Criddle AJ, Thélin P, Bussy F (2007) Pizgrischite, (Cu, Fe)$C_{u1}4PbB_{i1}7_{S3}5$, a new sulfosalt from the swiss alps: description, crystal structure and occurrence. Can Mineral 45:1229–1245

Meng E, Liu FL, Shi JR, Cai J, Cui Y (2013) Zircon U-Pb chronology, geochemistry of the previously “Pre-Sinian” intrusive rocks in Dandong area of southeastern Liaoning Province, and its tectonic implications. Acta Petrol Sin 29:421–436 (in Chinese with English abstract)

Mills SE, Tomkins AG, Weinberg RF, Fan HR (2015) Implications of pyrite geochemistry for gold mineralisation and remobilisation in the Jiaodong gold district, northeast China. Ore Geol Rev 71:150–168

Missen OP, Ram R, Mills SJ, Etschmann B, Reith F, Shuster J, Smith DJ, Brugger J (2020) Love is in the Earth: A review of tellurium (bio)geochemistry in surface environments. Earth-Sci Rev 204(103150):1–30

Mueller AG, Hagemann SG, Brugger J, Xing YL, Roberts MP (2020) Early Fimiston and late Oroya Au-Te ore, Paringa South mine, Golden Mile, Kalgoorlie: 4. Mineralogical and thermodynamic constraints on gold deposition by magmatic fluids at 420–300 ˚C and 300 MPa. Mineral Deposita 55:767–796

Oberthür T, Weiser TW (2008) Gold-bismuth-telluride-sulphide assemblages at the Viceroy Mine, Harare-Bindura-Shamva greenstone belt, Zimbabwe. Mineral Mag 72:953–970

Okamoto K, Tanner LE (1990) Bi-Te (bismuth-tellurium). In Massalski TB, Ohamoto K (eds) Binary alloy phase diagrams. ASM International, Materials Park, Ohio, 800–801

Okamoto H, Massalski TB (1983) The Au-Bi (gold-bismuth) system. Bull Alloy Phase Diagr 4:401–407

Okamoto H, Massalski TB (1986) Au-Te (gold-tellurium): American Society for Metals. Ohio 1:322–323

Pankratz LB (1982) Thermodynamic properties of elements and oxides. U.S. Bureau of Mines Bulletin, 672

Ponyatovskii EG (1960) The P-T diagram of bismuth at pressures of up to 30,000 kg/cm^2. Soviet Physics Crystallography 5:147–149

Prince A, Raynor GV, Evans DS (1990) Phase diagrams of ternary gold alloys. The Institute of Metals, London, p 505

Robie RA, Hemingway BS (1995) Thermodynamic properties of minerals and related substancies of 298.15 K and 1 bar (10^5 pascals) pressure and at higher temperatures. USGS Bulletin 2131, 461

Saunders JA, Brueseke ME (2012) Volatility of Se and Te during subduction-related distillation and the geochemistry of epithermal ores of the western United States. Econ Geol 107:165–172

Sparks HA, Mavrogenes JA (2005) Sulfide melt inclusions as evidence for the existence of a sulfide partial melt at Broken Hill, Australia. Econ Geol 100:773–779

Spence-Jones CP, Jenkin GRT, Boyce AJ, Hill NJ, Sangster CJS (2018) Tellurium, magmatic fluids and orogenic gold: An early magmatic fluid pulse at Cononish gold deposit, Scotland. Ore Geol Rev 102:894–905

Tomkins AG, Mavrogenes JA (2002) Mobilization of gold as a polymetallic melt during pelite anatexis at the Challenger deposit, South Australia: A metamorphosed Archean gold deposit. Econ Geol 97:1249–1271

Tomkins AG, Pattison DRM, Zaleski E (2004) The Hemlo gold deposit, Ontario: An example of melting and mobilization of a precious metal-sulfosalt assemblage during amphibolite facies metamorphism and deformation. Econ Geol 99:1063–1084

Tomkins AG, Pattison DRM, Frost BR (2007) On the initiation of metamorphic sulfide anataxis. J Petrol 48:511–536

Tomkins AG, Weinberg RF, McFarlane CRM (2009) Preferential magma extraction from K- and metal-enriched source regions in the crust. Mineral Deposita 44:171–181

Tomkins AG, Rebryna KC, Weinberg RF, Schaefer BF (2012) Magmatic sulfide formation by reduction of oxidized arc basalt. J Petrol 53:1537–1567

Tooth B, Brugger J, Ciobanu CL, Liu WH (2008) Modeling of gold scavenging by bismuth melts coexisting with hydrothermal fluids. Geol 36:815–818

Tooth B, Ciobanu CL, Green L, O'Neill B, Brugger J (2011) Bi-melt formation and gold scavenging from hydrothermal fluids: An experimental study. Geochim Cosmochim Acta 75:5423–5443

Tooth B, Etschmann B, Pokrovski GS, Testemale D, Hazemann JL, Grundler PV, Brugger J (2013) Bismuth speciation in hydrothermal fluids: an X-ray absorption spectroscopy and solubility study. Geochim Cosmochim Acta 101:156–172

Törmänen TO, Koski RA (2005) Gold enrichment and the Bi-Au association in pyrrhotite-rich massive sulfide deposits, Escanaba trough, Southern Gorda Ridge. Econ Geol 100:1135–1150

Voronin MV, Osadchii EG (2013) Thermodynamic properties of silver and bismuth sulfosalt minerals, pavonite ($AgBi_3S_5$) and matildite ($AgBiS_2$). Econ Geol 108:1203–1210

Voudouris PC, Spry PG, Mavrogonatos C, Sakellaris G, Bristol SK, Melfos V, Fornadel AP (2013) Bismuthinite derivatives, lillianite homologues, and bismuth sulfotellurides as indicators of gold mineralization in the Stanos shear-zone related deposit, Chalkidiki, northern Greece. Can Mineral 51:119–142

Wagner T (2007) Thermodynamic modeling of Au–Bi–Te melt precipitation from high temperature hydrothermal fluids: preliminary results. In Andrew CJ (ed) Mineral Exploration and Research: Digging Deeper. Proceedings of the 9th Biennial SGA Meeting, Irish Association of Economic Geologists, Dublin, 769–772

Wang YZ, Wang F, Wu L, Shi WB, Yang LK (2018) (U-Th)/He thermochronology of metallic ore deposits in the Liaodong Peninsula: Implications for orefield evolution in northeast China. Ore Geol Rev 92:348–365

Wei JH, Liu CQ, Zhao YX, Li ZD (2001) Time span of the ore-forming stages of the Wulong gold deposit, Liaoning. Geol Rev 47:433–437 (in Chinese with English abstract)

Wei B, Wang CY, Wang ZC, Cheng H, Xia XP, Tan W (2021) Mantle-derived gold scavenged by bismuth-(tellurium)-rich melts: evidence from the Mesozoic Wulong gold deposit in the North China Craton. Ore Geol Rev 131:104047

Wu FY, Lin JQ, Wilde SA, Zhang XO, Yang JH (2005) Nature and significance of the Early Cretaceous giant igneous event in eastern China. Earth Planet Sci Lett 233:103–119

Wu FY, Yang JH, Wilde SA, Zhang XO (2005) Geochronology, petrogenesis and tectonic implications of Jurassic granites in the Liaodong Peninsula, NE China. Chem Geol 221:127–156

Wu FY, Yang JH, Xu YG, Wilde SA, Walker RJ (2019) Destruction of the North China Craton in the Mesozoic. Annu Rev Earth Planet Sci 47:173–195

Xiao SY, Zhu G, Zhang S, Liu C, Su N, Yin H, Wu XD, Li YJ (2018) Structural processes and dike emplacement mechanism in the Wulong gold field, eastern Liaoning. Chin Sci Bull 63:3022–3036 (in Chinese with English abstract)

Xu WG, Fan HR, Hu FF, Santosh M, Yang KF, Lan TG, Wen BJ (2014) Gold mineralization in the Guilaizhuang deposit, southwestern Shandong Province, China: Insights from phase relations among sulfides, tellurides, selenides and oxides. Ore Geol Rev 56:276–291

Yang JH, Sun JF, Chen FK, Wilde SA, Wu FY (2007) Sources and Petrogenesis of Late Triassic gabbro Dikes in the Liaodong Peninsula: Implications for Post-collisional Lithosphere Thinning of the Eastern North China Craton. J Petrol 48:1973–1997

Yang JH, Wu FY, Wilde SA, Liu XM (2007) Petrogenesis of Late Triassic granitoids and their enclaves with implications for post-collisional lithospheric thinning of the Liaodong Peninsula, North China Craton. Chem Geol 242:155–175

Yang JH, Wu FY, Wilde SA, Belousova E, Griffin WL (2008) Mesozoic decratonization of the North China block. Geol 36:467–470

Yang JH, Sun JF, Zhang JH, Wilde SA (2012) Petrogenesis of Late Triassic intrusive rocks in the northern Liaodong Peninsula related to decratonization of the North China Craton: Zircon U-Pb age and Hf–O isotope evidence. Lithos 153:108–128

Yang L, Wang Q, Liu X (2015) Correlation between mineralization intensity and fluid–rock reaction in the Xinli gold deposit, Jiaodong Peninsula, China: Constraints from petrographic and statistical approaches. Ore Geol Rev 71:29–39

Yang LQ, Deng J, Guo LN, Wang ZL, Li XZ, Li JL (2016a) Origin and evolution of ore fluid, and gold-deposition processes at the giant Taishang gold deposit, Jiaodong Peninsula, eastern China. Ore Geol Rev 72:585–602

Yang LQ, Deng J, Wang ZL, Guo LN, Li RH, Groves DI, Danyushevsky LV, Zhang C, Zheng XL, Zhao H (2016) Relationships between gold and pyrite at the Xincheng gold deposit, Jiaodong Peninsula, China: Implications for gold source and deposition in a brittle epizonal environment. Econ Geol 111:105–126

Yang LQ, Guo LN, Wang ZL, Zhao RX, Song MC, Zheng XL (2017) Timing and mechanism of gold mineralization at the Wang'ershan gold deposit, Jiaodong Peninsula, eastern China. Ore Geol Rev 88:491–510

Yang FC, Song YH, Yang JL, Shen X, Gu YC (2018) SHRIMP U-Pb age and geochemical characteristics of granites in Wulong-Sidaogou gold deposit, east Liaoning. Geotecton Metallog 5:941–954 (in Chinese with English abstract)

Yu B, Zeng QD, Frimmel HE, Wang YB, Guo WK, Sun GT, Zhou TC, Li JP (2018) Genesis of the Wulong gold deposit, northeastern North China Craton: Constraints from fluid inclusions, H-O-S-Pb isotopes, and pyrite trace element concentrations. Ore Geol Rev 102:313–337

Zeng QD, Chen RY, Yang JH, Sun GT, Yu B, Wang YB, Chen PW (2019) The metallogenic characteristic and exploring ore potential of the gold deposit in eastern Liaoning Province. Acta Petrol Sin 35:1939–1963 (in Chinese with English abstract)

Zhang XO (2002) Setting and timing of gold mineralization in the Jiadong and Liaodong Peninsulas, North China Craton. Ph.D. thesis, Curtin University of Technology, 151–176

Zhang S, Zhu G, Liu C, Li YJ, Su N, Xiao SY, Gu CC (2018) Strike-Slip Motion Within the Yalu River Fault Zone, NE Asia: The Development of a Shear Continental Margin. Tectonics 37:1771–1796

Zhang P, Kou LL, Zhao Y, Bi ZW, Sha DM, Han RP, Li ZM (2020) Genesis of the Wulong gold deposit, Liaoning Province, NE China: Constraints from noble gases, radiogenic and stable isotope studies. Geosci Front 11:547–563

Zhang QS, Yang ZS (1988) Early crust and mineral deposits of Liaodong Peninsula, China. Geological Publishing House, Beijing, 493 (in Chinese)

Zhao YS, Jin CZ, Guan GY (1994) A study on the relationship between bismuth minerals and gold mineralization in the Wulong gold deposit, Liaoning Province. Acta Mineral Sin 14:88–91 (in Chinese with English abstract)

Zhao GC, Wilde SA, Cawood PA, Sun M (2001) Archean blocks and their boundaries in the North China Craton: lithological, geochemical, structural and P-T path constraints and tectonic evolution. Precambrian Res 107:45–73

Zheng YF, Xu Z, Zhao ZF, Dai LQ (2018) Mesozoic mafic magmatism in North China: implications for thinning and destruction of cratonic lithosphere. Sci China Earth Sci 61:353–385

Zhou QF, Li SR, Chen HY, Song YB, Zhang YQ, Zhang XB, Cui JC (2011) Discovery and geological significance of telluride minerals in the Yinggezhaung gold deposit, Rushan, Jiaodong. Acta Petrol Sin 27:1847–1856 (in Chinese with English abstract)

Zhou ZJ, Chen YJ, Jiang SY, Zhao HX, Qin Y, Hu CJ (2014) Geology, geochemistry and ore genesis of the Wenyu gold deposit, Xiaoqinling gold field, Qinling orogen, southern margin of north China craton. Ore Geol Rev 59:1–20

Zhou ZJ, Chen YJ, Jiang SY, Hu CJ, Qin Y, Zhao HX (2015) Isotope and fluid inclusion geochemistry and genesis of the Qiangma gold deposit, Xiaoqinling gold field, Qinling orogen, China. Ore Geol Rev 66:47–64

Zhou HY, Sun XM, Fu Y, Lin H, Jiang LY (2016) Mineralogy and mineral chemistry of Bi-minerals: Constraints on ore genesis of the Beiya giant porphyry-skarn gold deposit, southwestern China. Ore Geol Rev 79:408–424

Zhou HY, Sun XM, Cook NJ, Lin H, Fu Y, Zhong R, Brugger J (2017) Nano- to micron-scale particulate gold hosted by magnetite: A product of gold scavenging by bismuth melts. Econ Geol 112:993–1010

Zhou HY, Sun XM, Wu ZW, Yang TJ, Li DS, Ren YZ, Liu QF, Zhu KJ, Yu HJ (2018) Mineralogy of Bi-sulfosalts and tellurides from the Yaoan gold deposit, southwest China: metallogenic implications. Ore Geol Rev 98:126–140

Zhu RX, Chen L, Wu FY, Liu JL (2011) Timing, scale and mechanism of the destruction of the North China craton. Sci China Earth Sci 547:89–97

Zhu RX, Fan HR, Li JW, Meng QR, Li SR, Zeng QD (2015) Decratonic gold deposits. Sci China Earth Sci 58:1523–1537

Zhu RX, Zhang HF, Zhu G, Meng QR, Fan HR, Yang JH, Wu FY, Zhang ZY, Zheng TY (2017) Craton destruction and related resources. Int J Earth Sci 106:2233–2257